Summer 2024

Parametric Analysis of a Dynamic and Static Model for Low Velocity Impact of Specially Orthotropic Laminates

Juan Daniel Ruiz
University of Texas at Arlington

Parametric Analysis of a Dynamic and Static Model for Low Velocity Impact of Specially Orthotropic Laminates

by

Juan Ruiz

Thesis

Submitted in partial fulfilment of the requirements

for the degree of Master of Science in Aerospace Engineering at

The University of Texas at Arlington

August, 2024

Arlington, Texas

Supervising Committee:

Dr. Paul Davidson, Supervising Professor

Dr. Seiichi Nomura

Dr. Shiyao Lin

Dr. Xin Liu

Abstract

Parametric Analysis of a Dynamic and Static Model for Low Velocity Impact of Specially Orthotropic Laminates

The high specific strength and specific stiffness of composite materials makes them highly desirable for structural applications, but their laminated nature makes them susceptible to impact damage. Even low velocity impacts (LVI), generally, result in barely visible impact damage (BVID) and delamination, which can go unnoticed and grow during service, eventually leading to catastrophic failure. Due to this, the study of impact resistance and damage tolerance is typically studied through LVI followed by compression after impact (CAI) experiments. However, conducting LVI experiments are time consuming and expensive, as they require specialized equipment and extensive pre-test preparations.

In this study, the possibility of using quasi-static indentation experiments to replace dynamic impact testing is explored for specially orthotropic laminates. Analytical models are used to compare the response of plates under quasi-static central point loads and dynamic impact loading. Quasi-static indentation is modeled using first order shear deformation theory (FSDT), whereas the dynamic impact is modeled using a non-linear two degree of freedom spring mass model. Parametric analyses were conducted to study the influence of aspect ratio, laminate plate stiffness, and impact energy on feasible range where quasi-static indentation can replace dynamic impact tests.

ACKNOWLEDGEMENTS

I would like to express my thanks to Dr. Davidson for his constant support and guidance in writing this thesis. His guidance and insight throughout the research process has been a tremendous aid when I was uncertain about how to proceed. I would also like to thank him for his patience when working with me when progress was slow and uncertain.

I would also like to thank my family and friends for their constant support and encouragement to pursue this opportunity. Thank you to my parents for their constant love and support, and for always believing in me. Thank you to my friends for always being there for me when times are difficult.

Contents

List of Figures

List of Tables

Chapter 1

Introduction

1.1 Background

Low velocity impact (LVI) of composite structures has been a long running research effort for many years. Since 1960 to the present, the number of research papers related to the subject has grown to the tens of thousands and new research papers are continuing to be published every year. The high specific strength and specific stiffness of composite materials makes them highly desirable for structural applications, but their laminated nature makes them susceptible to impact damage. Even under low velocity impacts (LVI), barely visible impact damage (BVID) and delaminations can occur which can go unnoticed and grow, eventually leading to catastrophic failure. The main damage mechanisms of impact are fiber splitting, matrix cracking, and delamination, with delamination being the most critical. Delamination can cause a significant reduction in the compressive strength of the material [3]. Because of this, the study of impact resistance and damage tolerance is typically studied through low velocity impacts followed by compression after impact (CAI) experiments.

However, extensive studies of impacts on composite materials can be difficult to perform because of the numerous variables involved in the impact response and damage formation. These variables include the material properties of the composite, the impactor, laminate dimensions, boundary conditions, and the impact conditions. Extensive

preparation must also be taken to prepare samples for impact to ensure repeatability in the collected data. Alternatives to extensive impact studies may include sophisticated finite element analysis, but even this presents its own challenges. It is not unheard of for high fidelity FEM models with material damage to take over a day to run [8]. Because of the limitations associated with LVI testing, it is desirable to know if there are any circumstances under which impact testing can be replaced with inexpensive static indentation testing.

1.2 Objectives

The objective of this research paper is to compare the dynamic and static indentation models of composite laminates and to determine under what conditions the dynamic and static models produce similar results. Under the regions of similar responses, dynamic impact testing may potentially be substituted with static indentation. Analytical models for impact and indentation of simply supported and specially orthotropic laminates are to be studied. Additionally, as will be discussed later, a guideline for when membrane stiffening becomes significant will be set. Lastly, the possibility of inducing first ply delamination using static indentation within the linear response region is to be explored.

1.3 Thesis Outline

Chapter 2 presents a literature review on the subject of low velocity impacts of composite laminates and of the different types of analytical models used to describe them. In Chapter 3, impact characterization is introduced and the the dynamic and static indentation models involved in the study are described in detail and are compared against one another. Limitations of the static model used in this study are discussed. The setup of the parametric study is also presented in chapter 3. Chapter 4 presents the effects of changing parameters on the stiffening point and on the critical impact energy at which membrane effects occurs. Furthermore, in chapter 4, the applicability of static indentation for initiating first ply delamination is presented. The conclusion of the study and

recommendations for future work are presented in chapter 5.

Chapter 2

Literature Review

2.1 Low Velocity Impacts

A low velocity impact (LVI) is any event that involves an object striking a composite surface at a low velocity. A generally accepted velocity range for a low velocity impacts is between 0 and 10 m/s [1]. These events can result from a tool drop during manufacturing or maintenance, hail, or runway debris. LVI's are a significant field of research because of the failure modes that can occur during impact. Visible damages that can occur at the surface of impact include dent formation, fibre splitting, or cracks on the opposite side of impact. Barely visible impact damages (BVID) can include delamination or subsurface microcracks. These BVID can go unnoticed and can severely reduce the strength of the material. These damages can grow within the structure eventually leading to sudden failure.

The most common method of out-of-plane impact testing is the ASTM D7136/D7136M standard [9]. The method can be used for testing impact damage resistance or for inducing damage for further testing. The method involves drop loading a hemispherical tip impactor onto a composite laminate. The laminate boundary conditions can include corner clamped, circular clamped, simply supported, or any other boundary condition. The impactor mass or height can be adjusted to adjust the impact velocity and impact energy. Laminate test specimen dimensions are generally 100 mm by 150 mm and the

impactor generally has a mass of about 5.5 kg and a hemispherical striker tip with a 16 mm diameter. The impact force history and displacement history are collected for further analysis. A schematic of the drop testing is shown below.

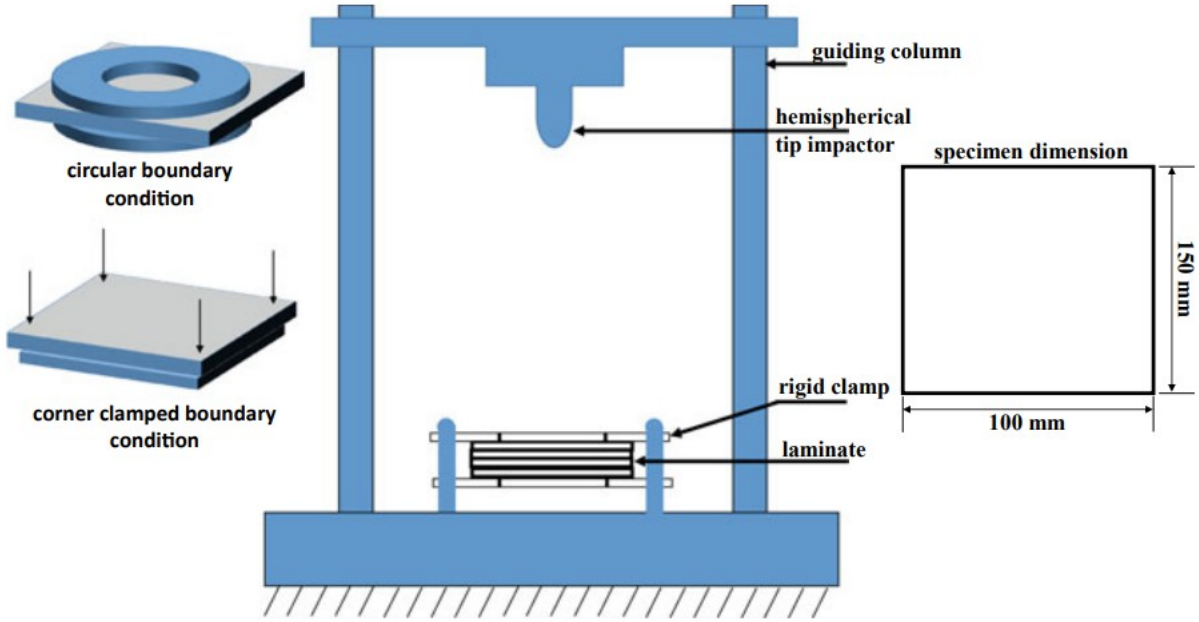

Figure 2.1: ASTM D7136/D7136M Testing [1]

In a series of impacts tests followed by compression after impact, Seamone et al. [3] showed that thick laminates could lose as much as 60% of their peak compressive load carrying capability without showing any barely visible impact damage. For thin laminates, the losses in compressive strength were much less significant, at around 17% prior to showing signs of BVID.

2.2 Categories of Analytical Impact Models

Analytical impact models can be powerful foundational tool for studying low velocity impacts. For certain categories of impacts, analytical models can provide quick and accurate solutions before engaging in more detailed and time consuming analysis. Abrate [10] states that there are three major categories of analytical models. These are the energy balance models, spring mass models, and complete models.

2.2.1 Energy Balance Models

In the case of quasi-static impacts, an energy balance model can be used to predict the maximum impact force and deflection. Assuming the impact is elastic and neglecting surface friction and material damping, the full kinetic energy of the impactor is used to deform the structure. In this case, the model can be solved by balancing the kinetic energy of the impactor with the energy stored in the bending stiffness, shear stiffness, membrane stiffness, and contact region [10].

$$\frac{1}{2}M_I V_0^2 = E_b + E_s + E_m + E_c \tag{2.1}$$

In the case of a half-space response, the maximum impact force and contact duration can easily be solved for [10]

$$P = \left(\frac{5}{4}\right)^{3/5} [M_I^3 V_0^6 k^2]^{1/5} \tag{2.2}$$

$$T_C = 3.2145 \left[\frac{M_I^2}{V_0 k^2}\right]^{1/5} \tag{2.3}$$

Energy balance models can can be used to predict maximum impact force and deflection, but cannot give force history or deflection history. When it is desirable to know these properties, spring mass models can be used in place of energy balance models.

2.2.2 Spring Mass Models

In the most complete spring mass model, the impact event is approximated as two masses connected by springs. These springs are the contact stiffness, bending stiffness, shear stiffness, and nonlinear membrane stiffness. A depiction of the two degree of freedom spring mass model is shown in Figure 2.2.

Using this model, the motion of the impactor, deflection of the plate, and the forces experienced by the impactor and plate can be predicted by solving the associated governing equations. The two degree of freedom spring mass model can be simplified for certain

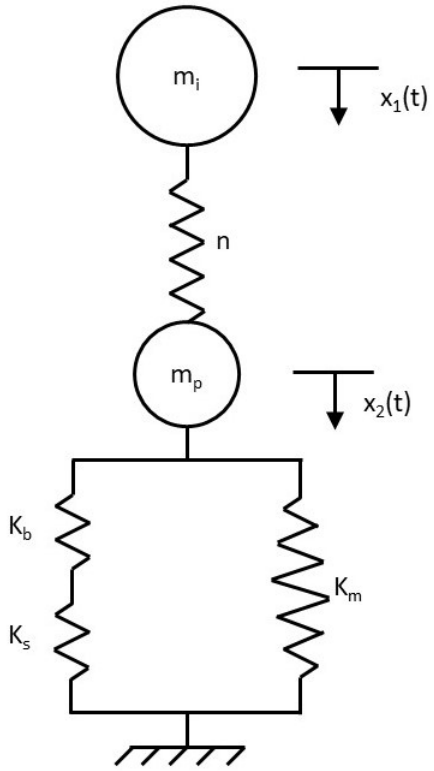

Figure 2.2: Two degree of freedom spring mass model

cases. In cases where the impactor mass is at least 3.5 times greater than the plate mass, the mass of the impactor will dominate the response and the plate mass can be neglected, reducing the 2 degree of freedom model to a single degree of freedom model [4] as shown in Figure 2.3.

In cases where thin plates are used, the shear stiffness can be neglected reducing the number of springs. The spring stiffnesses can determined either from analytical equations or from FEM using curve fitting of the force-deflection plots. [10] .

Spring mass models are useful because of their simplicity but can only give maximum plate deflection at the center of the plate. For additional information, such as the complete plate shape during deflection or internal stresses and strains experienced by the plate, complete models are needed.

2.2.3 Complete Models

The last category of analytical models are complete models, sometimes called full analytical models. Complete models begin with selecting the appropriate structural theory for

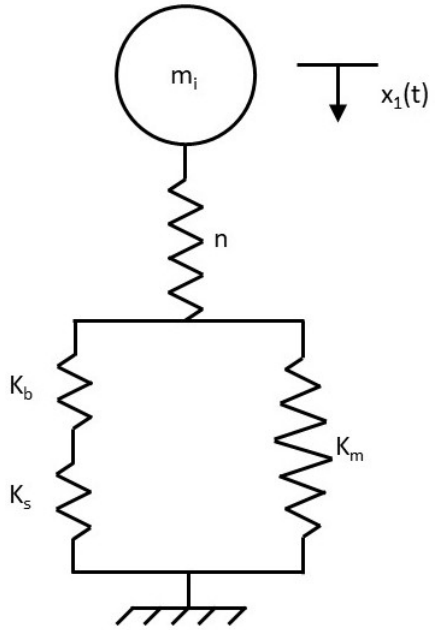

Figure 2.3: Single degree of freedom spring mass model

dynamic bending of a plate and solving the governing equations. As an example, consider the dynamic bending of a specially orthotropic plate governed by the first-ordered shear deformation theory [11].

$$D_{11}\frac{\partial^2\phi_x}{\partial x^2} + (D_{12}+D_{66})\frac{\partial^2\phi_y}{\partial x\partial y} + D_{66}\frac{\partial^2\phi_x}{\partial y^2} - KA_{55}\left(\phi_x + \frac{\partial w}{\partial x}\right) = I\ddot{\phi}_x \tag{2.4}$$

$$D_{22}\frac{\partial^2\phi_y}{\partial y^2} + (D_{12}+D_{66})\frac{\partial^2\phi_x}{\partial x\partial y} + D_{66}\frac{\partial^2\phi_y}{\partial x^2} - KA_{44}\left(\phi_y + \frac{\partial w}{\partial y}\right) = I\ddot{\phi}_y \tag{2.5}$$

$$KA_{55}\left(\frac{\partial\phi_x}{\partial x} + \frac{\partial^2 w}{\partial x^2}\right) + KA_{44}\left(\frac{\partial\phi_y}{\partial y} + \frac{\partial^2 w}{\partial y^2}\right) + P_z(x,y,t) = \rho h\ddot{w} \tag{2.6}$$

Pierson and Vaziri [11] solved this full analytical model based on the first-order shear deformation theory by approximating the impactor as a patch load over the center of the laminate and using a nonlinear Hertzian contact law. Their results showed the full analytical model to be as accurate as finite element software. These models can be very helpful because they are more computationally efficient than finite element software, but are are more complicated than spring mass models making them more difficult to use.

Chapter 3

Methodology

This chapter presents a detailed description of the analytical models used in this study. The governing equations are presented and the terms involved are explained. Use of the analytical models is validated through comparison with existing published results. The comparison procedure for determination of when the use of static models is acceptable is also explained.

3.1 Study Objectives

The objective of this study is to compare the responses of dynamic impact and static indentation models for the purpose of determining acceptable conditions where dynamic impact testing may be substituted with static indentation testing. As will be discussed, an additional goal of this study is to determine an acceptable level of deflection where membrane effects can be stated to be significant. In this study, large mass impacts are to be analyzed on a series of plates of varying thicknesses and area to determine how these parameters impact the dynamic and static responses and the onset of membrane effects.

3.2 Impact Characterization

One category of impacts that may allow static indentation testing to replace low velocity impact testing is the quasi-static impact. Low velocity impacts can be categorized using

2 dimensionless coefficients called the loss factor ζ, and the relative stiffness λ. Similar to how flow similarity can be equated using the Reynolds number, impact similarity can also be made using the loss factor and relative stiffness. The loss factor is a measure of how much impact energy is transferred to the plate. A large loss factor signifies a large amount of impact energy is transferred to the plate, whereas a small loss factor indicates only a small amount of energy is transferred to the plate. In conjunction with the relative stiffness, low velocity impacts can be categorized into four different groups. These groups are the infinite plate response, quasi-static response, half-space response, and impacts in the transition zone [12].

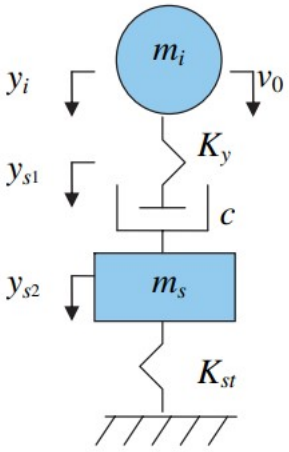

Figure 3.1: Lumped-Parameter Model [2]

Impact characterization is useful because it can give an understanding of what models are needed to model an impact. Impact characterization begins with establishing the asymptotic limits or extreme impact cases, and categorizing an impact between these limits. The goal is to determine the maximum non-dimensional force during impact as a function of the loss factor and relative stiffness. Consider a lumped parameter model of an impactor and structure or plate shown in Figure 3.1. From this model, Christofrou and Yigit [2] showed that the non-dimensional governing equations during contact can be written as

$$\ddot{\bar{\alpha}} + \frac{\sqrt{m_i K_y}}{c}\dot{\bar{\alpha}} + \bar{\alpha} + \ddot{\bar{y}}_{s2} = 0 \tag{3.1}$$

$$\ddot{\bar{y}}_{s2} + \frac{K_{st}}{K_y}\frac{m_i}{m_s}\bar{y}_{s2} = \frac{m_i}{m_s}\bar{\alpha} \tag{3.2}$$

$$\bar{F}(\bar{t}) = \bar{\alpha} \tag{3.3}$$

where $\bar{t} = \omega t$, $\bar{\alpha} = \frac{\alpha}{v_0/\omega}$, and $\omega = \sqrt{K_y/m_i}$ are the normalized time, indentation, and contact frequency. K_y is the contact stiffness given by

$$K_y = 5.2 r_i Y_c \tag{3.4}$$

where r_i is the impactor radius and Y_c is the compressive strength of the laminate. Now consider the case where the structure or plate mass is significantly larger than the impactor mass, and the mass ratio approaches zero ($m_i/m_s = \mu \to 0$). When this occurs, the plate structural dynamics can be neglected ($\ddot{\bar{y}}_{s2} = 0$) and the governing equation can be re-written as

$$\ddot{\bar{\alpha}} + 2\zeta\dot{\bar{\alpha}} + \bar{\alpha} = 0, \qquad \bar{\alpha}(0) = 0, \qquad \dot{\bar{\alpha}}(0) = 1 \tag{3.5}$$

where the loss factor ζ is given by

$$\zeta = \frac{\sqrt{m_i K_y}}{2c}, \quad c = 8\sqrt{\rho h D^*}, \quad \zeta = \frac{1}{16}\sqrt{\frac{m_i K_y}{\rho h D^*}} \tag{3.6}$$

where ρ is the laminate density and h is the laminate thickness. $D*$ is the effective plate stiffness given by

$$D^* = \sqrt{D_{11}D_{22}(A+1)/2} \quad A = (D_{12} + 2D_{66})/\sqrt{D_{11}D_{22}} \tag{3.7}$$

Equation 3.5 governs the response for the infinite plate as a function of only the loss factor. Using Equation 3.3, the normalized indentation can be related to the non-dimensional force and the solution to Equation 3.5 is

$$\bar{F}(\bar{t}) = \left\{ \begin{array}{ccc} \frac{e^{-\zeta\bar{t}}}{\sqrt{1-\zeta^2}} \sin\sqrt{1-\zeta^2}\bar{t} & \text{if} & \zeta < 1 \\ \bar{t}e^{-\bar{t}} & \text{if} & \zeta = 1 \\ \frac{1}{2\sqrt{\zeta^2-1}}(e^{(-\zeta+\sqrt{\zeta^2-1})\bar{t}} - e^{(-\zeta-\sqrt{\zeta^2-1})\bar{t}}) & \text{if} & \zeta > 1 \end{array} \right\} \quad \bar{t} = \omega t \tag{3.8}$$

The derivative of Equation 3.8 can be solved for to determine the time at which the maximum non-dimensional impact force occurs for the infinite plate response.

$$\bar{t}_{\max} = \left\{ \begin{array}{ccc} \frac{\tan^{-1}\sqrt{1-\zeta^2}/\zeta}{\sqrt{1-\zeta^2}} & \text{if} & \zeta < 1 \\ 1 & \text{if} & \zeta = 1 \\ \frac{1}{2\sqrt{\zeta^2-1}} \ln\frac{\zeta+\sqrt{\zeta^2-1}}{\zeta-\sqrt{\zeta^2-1}} & \text{if} & \zeta > 1 \end{array} \right\} \quad \bar{t} = \omega t \tag{3.9}$$

Now consider the opposite case where the impactor mass is significantly larger than the plate mass ($m_i/m_s = \mu \to \infty$). When this occurs, the inertia of the impactor will dominate the response and the governing equation can be written as [12]

$$(1+\lambda^{-1})\ddot{\bar{\alpha}} + \bar{\alpha} = 0, \qquad \bar{\alpha}(0) = 0, \qquad \dot{\bar{\alpha}}(0) = \lambda(1+\lambda)^{-1} \tag{3.10}$$

where the relative stiffness λ is the ratio of the plate structural stiffness to the contact stiffness, $\lambda = K_{st}/K_y$. The plate structural stiffness can be approximated as

$$K_{st} = \frac{D*}{0.0116\,(min(a,b))^2} \tag{3.11}$$

where $min(a,b)$ refers to the smaller side length dimension of the laminate. The solution for the quasi-static response giving the non-dimensional force during impact is given by

$$\bar{F}(\bar{t}) = \sqrt{\frac{\lambda}{1+\lambda}} \sin\sqrt{\frac{\lambda}{1+\lambda}}\bar{t} \tag{3.12}$$

The relative stiffness λ can be related to the loss factor ζ by the following equation [2]

$$\lambda = \frac{0.068\mu}{\zeta^2}, \qquad \mu = \frac{m_i}{m_s} \tag{3.13}$$

Using Equation 3.13, the maximum force of a quasi-static impact can be determined as a function of the loss factor

$$\bar{F}_{\max} = \sqrt{\frac{\lambda}{1+\lambda}} \tag{3.14}$$

$$\bar{F}_{\max} = \sqrt{\frac{0.068\mu/\zeta^2}{1+0.068\mu/\zeta^2}} = \sqrt{\frac{0.068\mu}{0.068\mu+\zeta^2}} \tag{3.15}$$

A suggested lower boundary value for the quasi-static impact is $\mu = 10$ [2].

$$\bar{F}_{\max} = \sqrt{\frac{0.68}{0.68+\zeta^2}} \tag{3.16}$$

By using Equations 3.8, 3.9 and 3.16, the asymptotic limits of the infinite plate response and quasi-static response can be plotted as functions of the loss factor as shown in Figure 3.2

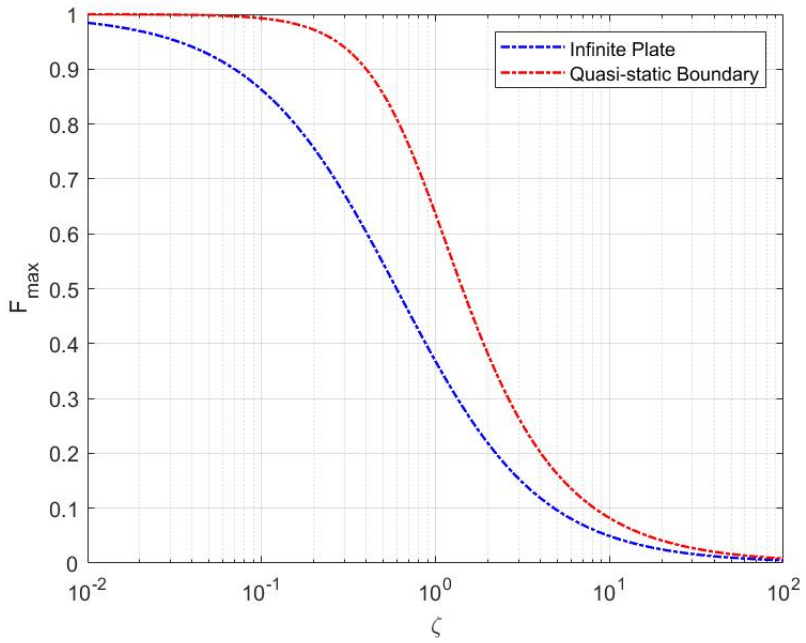

Figure 3.2: Impact Characterization Diagram: Dimensionless maximum impact force $\bar{F}_{\max}$ vs. loss factor ζ

Now for any impact, the maximum force during impact can be predicted using Equation 3.14 or Equation 3.15 and plotted on Figure 3.2 using the predicted force and the loss factor. Any impacts plotted near the infinite plate boundary curve can be modeled using the infinite plate response. Any impacts plotted to the right of the quasi-static boundary curve can be modeled as quasi-static impacts. Impacts plotted between the two curves fall under a transition zone and will require complete models to analyze [2].

During a quasi-static impact, flexural waves originating from the location of impact will travel many times over throughout the structure in all directions. This allows the structure or plate to behave as if it is deforming under a static load and can be modeled using either an energy balance approach, a spring mass model, or a complete model if desired [10]. In the case of the infinite plate response, the contact duration is sufficiently short such that there is insufficient time for the flexural waves to travel to the plate boundaries, and the response is controlled by wave propagation [13]. When the impact duration is sufficiently long enough for flexural waves to reach the plate boundaries, but short enough that flexural waves travel back and forth only a few times, the impact falls under the transition zone between the infinite plate response and the quasi-static response [2].

Finally, for completeness, the last category of impacts is the half-space response. This response is shown to occur when the impactor mass is sufficiently small ($\zeta \to 0, \mu \to 0$) such that the response can be approximated by the half-space solution and Equation 3.5 becomes

$$\ddot{\bar{\alpha}} + \bar{\alpha} = 0 \tag{3.17}$$

In a half-space response, the vibration of the plate is mostly negligible and there is no significant structural deflection. Instead, the impact response is localized in the contact region, meaning only local contact deflection occurs. Impacts which approach a maximum non-dimensional force of 1 on the characterization diagram can be modeled using the half-space response.

3.3 Nonlinear Spring Mass Model

The dynamic impact model used here to describe the low velocity impact event is the one developed by Shivakumar [4]. This model can be used to predict the deflection and impact force for an isotropic, quasi-isotropic, or specially orthotropic and circular plate. The model can be used with simply supported or clamped boundary conditions. Despite being developed for circular plates, other researchers [3, 14, 15] have extended its use to rectangular plates by circular plates of equal area.

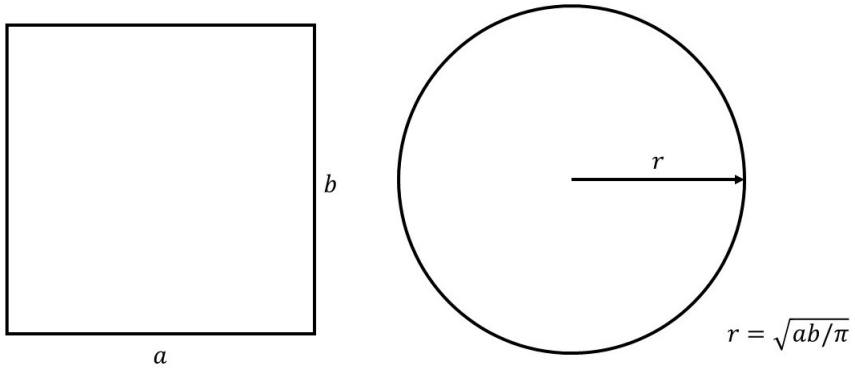

Figure 3.3: Square and Circular Plate of Equal Area

The model describes the motion of the impactor and plate as two masses connected by springs in the absence of material damping, plate damage, and surface friction. These springs are the contact stiffness, bending stiffness, shear stiffness, and membrane stiffness. A depiction of the two degree of freedom spring mass model was shown in Figure 2.2. The values of the bending and membrane stiffness are determined by the material properties of the plate and the boundary conditions. Expressions for the bending and membrane stiffness of a centrally loaded plate are shown in Table 3.1.

Here, h is the laminate thickness, r is the radius of the laminate, and E_r and ν_r are the average planar values for the Young's modulus and the Poisson's ratio. The determination of the bending and membrane stiffnesses assumes average planar values for the Young's modulus and Poisson's ratio. In the case of isotropic materials and quasi-isotropic laminates, this is true. In the case of specially orthotropic laminates, the Young's modulus and Poisson's ratio are dependent on the direction of the applied force. However, these values can be averaged across the surface of the material [15].

Boundary Conditions	Edge Conditions	Bending Stiffness K_b	Membrane Stiffness K_m
Clamped	Immovable	$\frac{4\pi E_r h^3}{3(1-\nu_r^2)r^2}$	$\frac{(353-191)\pi E_r h}{648(1-\nu_r)r^2}$
	Moveable	$\frac{4\pi E_r h^3}{3(1-\nu_r^2)r^2}$	$\frac{191\pi E_r h}{648r^2}$
Simply Supported	Immovable	$\frac{4\pi E_r h^3}{3(3+\nu_r)(1-\nu_r)r^2}$	$\frac{\pi E_r h}{(3+\nu_r)^4 a^2}(\frac{191}{648}(1+\nu_r)^4+\frac{41}{27}(1+\nu_r)^3+\frac{32}{9}(1+\nu_r)^2+\frac{40}{9}(1+\nu_r)+\frac{8}{3}+\frac{1}{1-\nu_r}[\frac{(1+\nu_r)^4}{4}+2(1+\nu_r)^3+8(1+\nu_r)^2+16(1+\nu_r)+16])$
	Moveable	$\frac{4\pi E_r h^3}{3(3+\nu_r)(1-\nu_r)r^2}$	$\frac{\pi E_r h}{(3+\nu_r)^4 a^2}(\frac{191}{648}(1+\nu_r)^4+\frac{41}{27}(1+\nu_r)^3+\frac{32}{9}(1+\nu_r)^2+\frac{40}{9}(1+\nu_r)+\frac{8}{3})$

Table 3.1: Bending and Membrane Stiffness of Centrally Loaded Plates [4]

$$E_r = \frac{1}{2\pi}\int_0^{2\pi} E(\theta)d\theta \quad \nu_r = \frac{1}{2\pi}\int_0^{2\pi} \nu(\theta)d\theta \tag{3.18}$$

The determination of the shear stiffness is much more involved than for the bending and membrane stiffness. The bending and membranes stiffness are constant but the shear stiffness is a function of the applied loading and must be solved iteratively for each new load. The shear stiffness is given by

$$K_s = \frac{4\pi G_{zr} h}{3}\left(\frac{E_r}{E_r - 4\nu_{zr}G_{zr}}\right)\left(\frac{1}{4/3 + \ln r/r_c}\right) \tag{3.19}$$

where G_{zr} is the averaged shear modulus in the zr plane, ν_{zr} is the averaged Poisson's ratio in the zr plane, and r_c is the radius of the contact region. The radius of the contact region is given by

$$r_c = \left[\frac{3\pi}{4}P(K_1+K_2)r_i\right]^{1/3} \tag{3.20}$$

where P is the applied force and K_1 and K_2 are constants to be determined.

$$K_1 = \frac{1-\nu_i^2}{\pi E_i} \quad K_2 = \frac{\sqrt{A_{22}}[(\sqrt{A_{11}A_{22}}+G_{zr})^2-(A_{12}+G_{zr})^2]^{1/2}}{2\pi\sqrt{G_{zr}}(A_{11}A_{22}-A_{12}^2)} \tag{3.21}$$

and

$$\begin{gathered}\delta = E_r/E_z \qquad \beta = \frac{1}{1-\nu_r-2\nu_{zr}^2\delta} \\ A_{11} = E_z(1-\nu_r)\beta \quad A_{22} = \frac{E_r\beta(1-\nu_{zr}^2\delta)}{1+\nu_r} \quad A_{12} = E_r\nu_{zr}\beta\end{gathered} \tag{3.22}$$

For an isotropic impactor, E_i is the impactor's Young's modulus, ν_i is the impactor's Poisson's ratio, and E_z is the laminate's Young's modulus in the z direction. Once these expressions are solved for, the contact spring n can also be solved for.

$$n = \frac{4\sqrt{r_i}}{3\pi(K_1+K_2)} \tag{3.23}$$

Lastly, the governing equation for the low velocity impact is given by

$$\begin{gathered}m_i\ddot{x}_1 + \lambda n|x_1 - x_2|^{1.5} = 0 \\ m_p\ddot{x}_2 + K_{bs}x_2 + K_m x_2^3 - \lambda n|x_1 - x_2|^{1.5} = 0\end{gathered} \tag{3.24}$$

with initial conditions

$$x_1(0) = 0, \quad \dot{x}_1(0) = V_0, \quad x_2(0) = 0, \quad \dot{x}_2(0) = 0 \tag{3.25}$$

and

$$\begin{gathered}\lambda = 1 \quad \text{for} \quad x_1 > x_2 \\ \lambda = -1 \quad \text{for} \quad x_1 < x_2\end{gathered} \tag{3.26}$$

The dynamic model produces the impactor and plate deflection as a function time. From the plate deflection, the impact force can be determined at any moment using the equation below.

$$P = K_{bs}w + K_m w^3 \tag{3.27}$$

where w is the midplane deflection of the plate and is equal to x_2. Because the shear stiffness is a function of the applied loading, the governing equation must be solved iteratively at each step. Generic plots of the plate and impactor displacement and impact force are shown in Figure 3.4.

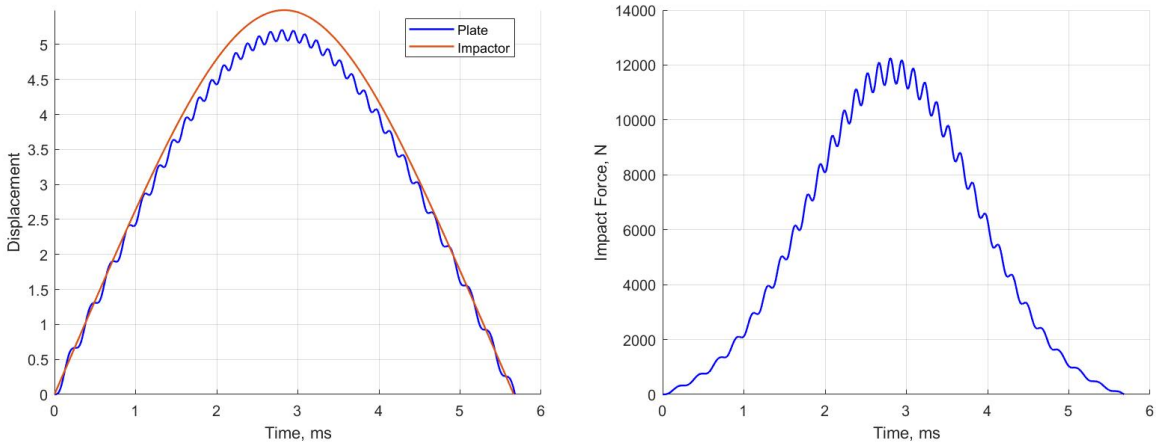

(a) Displacement Response (b) Impact Force Response

Figure 3.4: 2DOF Spring Mass Model System Outputs

These plots can then be combined to produce the force-deflection plot of the impact as shown in Figure 3.5

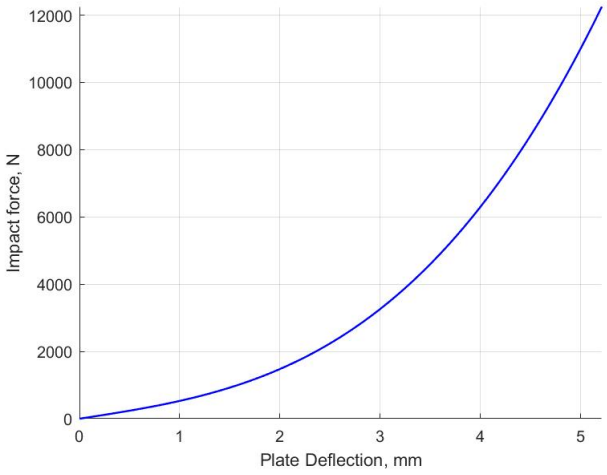

Figure 3.5: 2DOF Spring Mass Model Force-Deflection Plot

3.4 Validation of the Dynamic Impact Model

To ensure that the dynamic impact model is implemented correctly and is representative of real impacts, the results of the impact model are compared with available results in the literature. In his paper, Shivakumar [4] applied the 2 degree of freedom spring mass model to a clamped aluminum plate subject to a low velocity impact. His analysis is repeated here to ensure that the impact model is implemented correctly. Shown in Figure 3.6 are

both the displacement and impact force of the impact as predicted by the impact model and from Shivakumar's analysis.

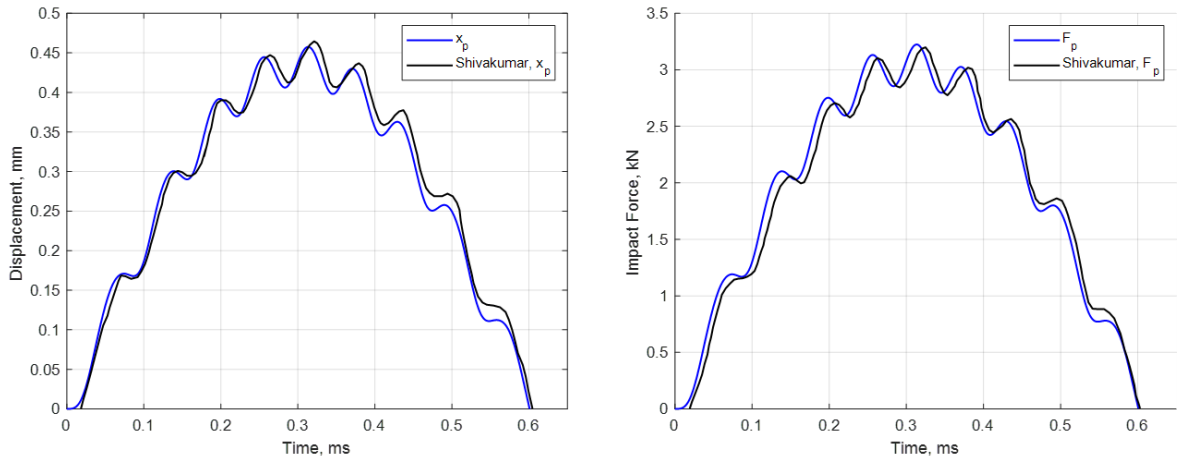

(a) Plate Displacement Response (b) Impact Force Response

Figure 3.6: Impact on a Clamped Aluminum Plate

The results from the model and Shivakumar's own results show good agreement giving confidence that the model is implemented correctly. In a separate study, Pierson [11] developed a complete analytical model using the first-order shear deformation theory. In his study, he conducted a low velocity impact on a quasi-isotropic rectangular plate to compare his analytical model with measured data. Both his predicted and measured results are shown in Figure 3.7.

There is some disagreement between the 2 degree of freedom spring mass model and Pierson's predicted and measured data. Some of this disagreement can be attributed to Pierson using a rectangular plate and the 2 DOF model being developed for circular plates. Still, overall the 2 DOF model captures the overall results fairly well.

3.5 Static Indentation using FSDT

The First-Order Shear Deformation Theory (FSDT) is an extension of the Classical Laminated Plate Theory (CLPT) in which the laminated plate is treated as a statically equivalent single layer reducing the 3-D continuum problem to a 2-D problem. Both theories are developed by assuming a form of the displacement field or stress field as a linear com-

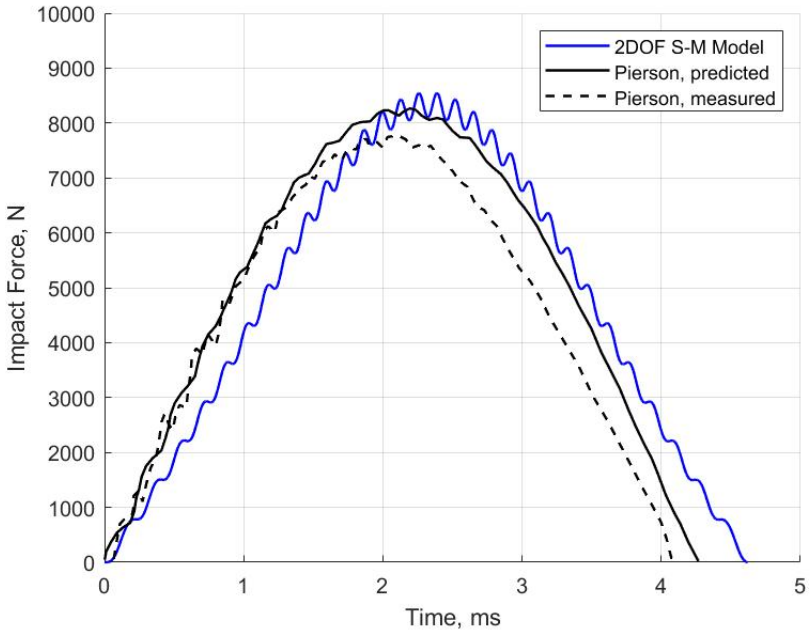

Figure 3.7: Impact on a Simply Supported Plate

bination of unknown functions and the thickness coordinate. Theses theories are termed the Equivalent Single Layer theories (ESL) and the simplest of which is the Classical Laminated Plate Theory. The displacement field of CLPT is shown below [16].

$$\begin{aligned} u(x,y,z,t) &= u_0(x,y,t) - z\frac{\partial w_0}{\partial x} \\ v(x,y,z,t) &= v_0(x,y,t) - z\frac{\partial w_0}{\partial y} \\ w(x,y,z,t) &= w_0(x,y,t) \end{aligned} \tag{3.28}$$

Where u_0, v_0, w_0 are the displacement components along the (x,y,z) coordinate directions of a point on the midplane. This displacement field implies

1. Straight lines perpendicular to the midsurface remain straight after deformation.
2. Transverse normals do not experience elongation.
3. Transverse normals rotate such that they remain perpendicular to the midsurface after deformation

Statements 1 and 2 state that the transverse displacement is independent of the z coordinate, and transverse normal strain / stress is zero. In other words, normal stress in

the z direction is zero. Statement 3 states that the transverse shear strain / shear stress is zero ($\sigma_{xz}, \sigma_{yz} = 0$). In the First-order Shear Deformation theory, statement 3 is relaxed and transverse normals are allowed to rotate about the midsurface after deformation but remain straight. The displacement field of FSDT is shown below [16].

$$\begin{aligned} u(x,y,z,t) &= u_0(x,y,t) + z\phi_x(x,y,t) \\ v(x,y,z,t) &= v_0(x,y,t) + z\phi_y(x,y,t) \\ w(x,y,z,t) &= w_0(x,y,t) \end{aligned} \tag{3.29}$$

In addition to the displacements u_0, v_0, w_0, the rotation angles ϕ_x, ϕ_y must also be determined. It should be noted that ϕ_x represents the rotation of the transverse normal about the y axis and ϕ_y represents the rotation of the transverse normal about the x axis. For thin plates (a/h > 20), CLPT can give an accurate solution to the out of plane bending problem. For relatively thick plates, the solution begin to lose accuracy. In these cases, FSDT can be used to provide a more accurate solution than CLPT. In FSDT, transverse stress / strains are no longer zero but are treated as constant throughout the thickness of the laminate. In reality, the shear strains vary at least quadratically through the layer thickness [16]. The discrepancy between the constant shear stress assumption and the actual shear stress state is corrected through use of a shear correction factor K. The calculation of the shear correction factor is difficult to perform because it depends on the laminate, loading, and boundary conditions. In general, a value of 5/6 is used in most of the literature [16] [11].

The equations of motion of the First order Shear Deformation Theory for a rectangular plate in terms of the generalized displacements (u_0, v_0, w_0, ϕ_x and ϕ_y) are [16]

$$\frac{\partial}{\partial x}\left[A_{11}\frac{\partial u_0}{\partial x}+A_{12}\frac{\partial v_0}{\partial y}+A_{16}\left(\frac{\partial u_0}{\partial y}+\frac{\partial v_0}{\partial x}\right)+B_{11}\frac{\partial \phi_x}{\partial x}+B_{12}\frac{\partial \phi_y}{\partial y}+B_{16}\left(\frac{\partial \phi_x}{\partial y}+\frac{\partial \phi_y}{\partial x}\right)\right]$$
$$+\frac{\partial}{\partial y}\left[A_{16}\frac{\partial u_0}{\partial x}+A_{26}\frac{\partial v_0}{\partial y}+A_{66}\left(\frac{\partial u_0}{\partial y}+\frac{\partial v_0}{\partial x}\right)+B_{16}\frac{\partial \phi_x}{\partial x}+B_{26}\frac{\partial \phi_y}{\partial y}+B_{66}\left(\frac{\partial \phi_x}{\partial y}+\frac{\partial \phi_y}{\partial x}\right)\right]$$
$$-\left(\frac{\partial N^T_{xx}}{\partial x}+\frac{\partial N^T_{xy}}{\partial y}\right)=I_0\frac{\partial^2 u_0}{\partial t^2}+I_1\frac{\partial^2 \phi_x}{\partial t^2} \quad (3.30)$$

$$\frac{\partial}{\partial x}\left[A_{16}\frac{\partial u_0}{\partial x}+A_{26}\frac{\partial v_0}{\partial y}+A_{66}\left(\frac{\partial u_0}{\partial y}+\frac{\partial v_0}{\partial x}\right)+B_{16}\frac{\partial \phi_x}{\partial x}+B_{26}\frac{\partial \phi_y}{\partial y}+B_{66}\left(\frac{\partial \phi_x}{\partial y}+\frac{\partial \phi_y}{\partial x}\right)\right]$$
$$+\frac{\partial}{\partial y}\left[A_{12}\frac{\partial u_0}{\partial x}+A_{22}\frac{\partial v_0}{\partial y}+A_{26}\left(\frac{\partial u_0}{\partial y}+\frac{\partial v_0}{\partial x}\right)+B_{12}\frac{\partial \phi_x}{\partial x}+B_{22}\frac{\partial \phi_y}{\partial y}+B_{26}\left(\frac{\partial \phi_x}{\partial y}+\frac{\partial \phi_y}{\partial x}\right)\right]$$
$$-\left(\frac{\partial N^T_{xy}}{\partial x}+\frac{\partial N^T_{yy}}{\partial y}\right)=I_0\frac{\partial^2 v_0}{\partial t^2}+I_1\frac{\partial^2 \phi_y}{\partial t^2} \quad (3.31)$$

$$\frac{\partial}{\partial x}\left[KA_{45}\left(\frac{\partial w_0}{\partial y}+\phi_y\right)+KA_{55}\left(\frac{\partial w_0}{\partial x}+\phi_x\right)\right]$$
$$+\frac{\partial}{\partial y}\left[KA_{44}\left(\frac{\partial w_0}{\partial y}+\phi_y\right)+KA_{45}\left(\frac{\partial w_0}{\partial x}+\phi_x\right)\right]$$
$$+\hat{N}_{xx}\frac{\partial^2 w_0}{\partial x^2}+2\hat{N}_{xy}\frac{\partial^2 w_0}{\partial x\partial y}+\hat{N}_{yy}\frac{\partial^2 w_0}{\partial y^2}+q(x,y)=I_0\frac{\partial^2 w_0}{\partial t^2} \quad (3.32)$$

$$\frac{\partial}{\partial x}\left[B_{11}\frac{\partial u_0}{\partial x}+B_{12}\frac{\partial v_0}{\partial y}+B_{16}\left(\frac{\partial u_0}{\partial y}+\frac{\partial v_0}{\partial x}\right)+D_{11}\frac{\partial \phi_x}{\partial x}+D_{12}\frac{\partial \phi_y}{\partial y}+D_{16}\left(\frac{\partial \phi_x}{\partial y}+\frac{\partial \phi_y}{\partial x}\right)\right]$$
$$+\frac{\partial}{\partial y}\left[B_{16}\frac{\partial u_0}{\partial x}+B_{26}\frac{\partial v_0}{\partial y}+B_{66}\left(\frac{\partial u_0}{\partial y}+\frac{\partial v_0}{\partial x}\right)+D_{16}\frac{\partial \phi_x}{\partial x}+D_{26}\frac{\partial \phi_y}{\partial y}+D_{66}\left(\frac{\partial \phi_x}{\partial y}+\frac{\partial \phi_y}{\partial x}\right)\right]$$
$$-\left[KA_{45}\left(\frac{\partial w_0}{\partial y}+\phi_y\right)+KA_{55}\left(\frac{\partial w_0}{\partial x}+\phi_x\right)\right]-\left(\frac{\partial M^T_{xx}}{\partial x}+\frac{\partial M^T_{xy}}{\partial y}\right)=I_2\frac{\partial^2 \phi_x}{\partial t^2}+I_1\frac{\partial^2 u_0}{\partial t^2}$$
(3.33)

$$\frac{\partial}{\partial x}\left[B_{16}\frac{\partial u_0}{\partial x}+B_{26}\frac{\partial v_0}{\partial y}+B_{66}\left(\frac{\partial u_0}{\partial y}+\frac{\partial v_0}{\partial x}\right)+D_{16}\frac{\partial \phi_x}{\partial x}+D_{26}\frac{\partial \phi_y}{\partial y}+D_{66}\left(\frac{\partial \phi_x}{\partial y}+\frac{\partial \phi_y}{\partial x}\right)\right]$$
$$+\frac{\partial}{\partial y}\left[B_{12}\frac{\partial u_0}{\partial x}+B_{22}\frac{\partial v_0}{\partial y}+B_{26}\left(\frac{\partial u_0}{\partial y}+\frac{\partial v_0}{\partial x}\right)+D_{12}\frac{\partial \phi_x}{\partial x}+D_{22}\frac{\partial \phi_y}{\partial y}+D_{26}\left(\frac{\partial \phi_x}{\partial y}+\frac{\partial \phi_y}{\partial x}\right)\right]$$
$$-\left[KA_{44}\left(\frac{\partial w_0}{\partial y}+\phi_y\right)+KA_{45}\left(\frac{\partial w_0}{\partial x}+\phi_x\right)\right]-\left(\frac{\partial M_{xy}^T}{\partial x}+\frac{\partial M_{yy}^T}{\partial y}\right)=I_2\frac{\partial^2 \phi_y}{\partial t^2}+I_1\frac{\partial^2 v_0}{\partial t^2} \tag{3.34}$$

where N_{xx}^T, N_{yy}^T, N_{xy}^T, M_{xx}^T, M_{yy}^T, and M_{xy}^T represent the thermal in-plane force resultants and moment resultants and I_0, I_1, and I_2 are the mass moments of inertia. The symbols A, B, and D with subscripts refer to components of the extensional stiffnesses $[A]$, bending stiffnesses $[D]$, and the bending-extensional coupling stiffnesses $[B]$. For derivations of these components, see [16]. For a specially orthotropic laminate

$$A_{16}=0,\ A_{26}=0,\ A_{45}=0,\ [B]=0,\ D_{16}=0,\ D_{26}=0,\ I_1=0 \tag{3.35}$$

For the static bending case of specially orthotropic laminates and in the absence of thermal resultants and in-plane forces or moments, considering only out of plane forces, the governing equations can be reduced to

$$A_{11}\frac{\partial^2 u_0}{\partial x^2}+A_{12}\frac{\partial^2 v_0}{\partial x \partial y}+A_{66}\left(\frac{\partial^2 u_0}{\partial y^2}+\frac{\partial^2 v_0}{\partial x \partial y}\right)=0 \tag{3.36}$$

$$A_{12}\frac{\partial^2 u_0}{\partial x \partial y}+A_{22}\frac{\partial^2 v_0}{\partial y^2}+A_{66}\left(\frac{\partial^2 u_0}{\partial x \partial y}+\frac{\partial^2 v_0}{\partial x^2}\right)=0 \tag{3.37}$$

$$KA_{55}\left(\frac{\partial^2 w_0}{\partial x^2}+\frac{\partial \phi_x}{\partial x}\right)+KA_{44}\left(\frac{\partial^2 w_0}{\partial y^2}+\frac{\partial \phi_y}{\partial y}\right)+q(x,y)=0 \tag{3.38}$$

$$D_{11}\frac{\partial^2 \phi_x}{\partial x^2}+(D_{12}+D_{66})\frac{\partial^2 \phi_y}{\partial x \partial y}+D_{66}\frac{\partial^2 \phi_x}{\partial y^2}-KA_{55}\left(\frac{\partial w_0}{\partial x}+\phi_x\right)=0 \tag{3.39}$$

$$D_{22}\frac{\partial^2\phi_y}{\partial y^2} + (D_{12} + D_{66})\frac{\partial^2\phi_x}{\partial x \partial y} + D_{66}\frac{\partial^2\phi_y}{\partial x^2} - KA_{44}\left(\frac{\partial w_0}{\partial y} + \phi_y\right) = 0 \tag{3.40}$$

where $q(x, y)$ represents the out of plane loading. Now consider a simply supported rectangular laminate subject to a central point load as shown in Figure 3.8.

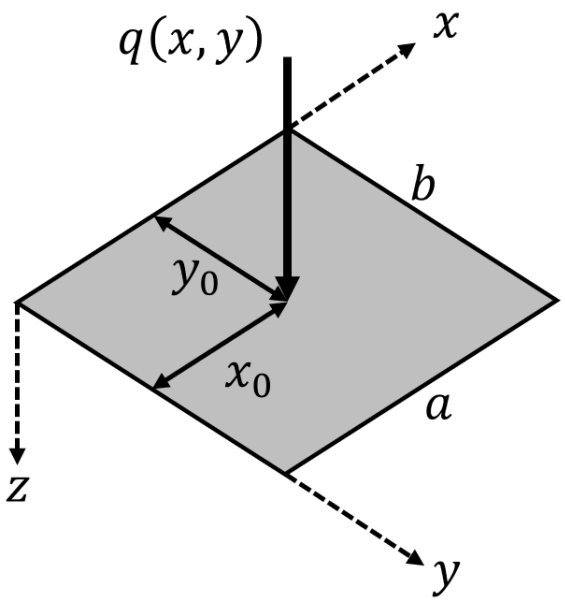

Figure 3.8: Central Point Loading of a Rectangular Laminate

For the case of simply supported boundary conditions, the edge conditions are

$$\begin{array}{llll} u_0(x,0) = 0, & u_0(x,b) = 0, & v_0(0,y) = 0, & v_0(a,y) = 0 \\ w_0(x,0) = 0, & w_0(x,b) = 0, & w_0(0,y) = 0, & w_0(a,y) = 0 \\ \phi_x(x,0) = 0, & \phi_x(x,b) = 0, & \phi_y(0,y) = 0, & \phi_y(a,y) = 0 \end{array} \tag{3.41}$$

$$\begin{array}{llll} N_{xx}(0,y) = 0, & N_{xx}(a,y) = 0, & N_{yy}(x,0) = 0, & N_{yy}(x,b) = 0 \\ M_{xx}(0,y) = 0, & M_{xx}(a,y) = 0, & M_{yy}(x,0) = 0, & M_{yy}(x,b) = 0 \end{array} \tag{3.42}$$

These conditions are satisfied by the following expansions [16]

$$u_0(x,y) = \sum_{n=1}^{\infty}\sum_{m=1}^{\infty} U_{mn}\cos\alpha x\ \sin\beta y \tag{3.43}$$

$$v_0(x,y) = \sum_{n=1}^{\infty}\sum_{m=1}^{\infty} V_{mn} \sin\alpha x \ \cos\beta y \tag{3.44}$$

$$w_0(x,y) = \sum_{n=1}^{\infty}\sum_{m=1}^{\infty} W_{mn} \sin\alpha x \ \sin\beta y \tag{3.45}$$

$$\phi_x(x,y) = \sum_{n=1}^{\infty}\sum_{m=1}^{\infty} X_{mn} \cos\alpha x \ \sin\beta y \tag{3.46}$$

$$\phi_y(x,y) = \sum_{n=1}^{\infty}\sum_{m=1}^{\infty} Y_{mn} \sin\alpha x \ \cos\beta y \tag{3.47}$$

where $\alpha = m\pi/a$, $\beta = n\pi/b$. The coefficients U_{mn}, V_{mn}, W_{mn}, X_{mn}, and Y_{mn} are given by

$$\begin{bmatrix} \hat{s}_{11} & \hat{s}_{12} & 0 & 0 & 0 \\ \hat{s}_{12} & \hat{s}_{22} & 0 & 0 & 0 \\ 0 & 0 & \hat{s}_{33} & \hat{s}_{34} & \hat{s}_{35} \\ 0 & 0 & \hat{s}_{34} & \hat{s}_{44} & \hat{s}_{45} \\ 0 & 0 & \hat{s}_{35} & \hat{s}_{45} & \hat{s}_{55} \end{bmatrix} \begin{Bmatrix} U_{mn} \\ V_{mn} \\ W_{mn} \\ X_{mn} \\ Y_{mn} \end{Bmatrix} = \begin{Bmatrix} 0 \\ 0 \\ Q_{mn} \\ 0 \\ 0 \end{Bmatrix} \tag{3.48}$$

where

$$\begin{gathered} \hat{s}_{11} = (A_{11}\alpha^2 + A_{66}\beta^2) \qquad \hat{s}_{12} = (A_{12} + A_{66})\,\alpha\beta \qquad \hat{s}_{22} = (A_{66}\alpha^2 + A_{22}\beta^2) \\ \hat{s}_{33} = K\,(A_{55}\alpha^2 + A_{44}\beta^2) \qquad \hat{s}_{34} = KA_{55}\alpha \qquad \hat{s}_{35} = KA_{44}\beta \\ \hat{s}_{44} = (D_{11}\alpha^2 + D_{66}\beta^2 + KA_{55}) \quad \hat{s}_{45} = (D_{12} + D_{66})\,\alpha\beta \quad \hat{s}_{55} = (D_{66}\alpha^2 + D_{22}\beta^2 + KA_{44}) \end{gathered} \tag{3.49}$$

The coefficients Q_{mn} represent the double fourier series expansion of the loading conditions. For a point load as depicted in Figure 3.8 located at (x_0, y_0), the coefficients are given by

$$Q_{mn} = \tfrac{4Q_0}{ab} \sin\tfrac{m\pi x_0}{a} \ \sin\tfrac{n\pi y_0}{b}, \qquad (m,n = 1,2,3,...) \tag{3.50}$$

The system of equations shown in Equation 3.48 can then be solved to determine the coefficients W_{mn} to solve for the center plate deflection using Equation 3.45.

3.5.1 Limitations of FSDT

FSDT can be useful for predicting out of plane bending, but it is limited to small deflections. Larger deflections create stretching of the plate which produces significant membrane forces. These membrane forces caused by stretching of the plate drastically increase the amount of force necessary to create additional bending [17]. In the two degree of freedom spring mass model, this is accounted for through the use of the nonlinear membrane stiffness K_m. However, the strain formulation for FSDT does not account for these forces and is only capable of producing linear force-deflection plots. Consider a 16 ply 2.08 mm thick specially orthotropic plate of 100 x 100 mm subject to a central point load. Using FSDT, a typical force-deflection plot would appear as shown in Figure 3.9

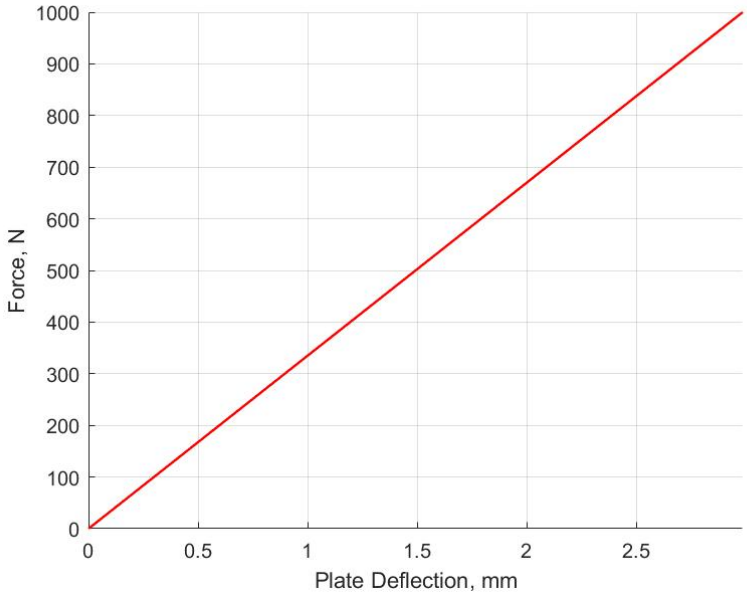

Figure 3.9: Force-Deflection Plot using FSDT

Despite the deflection exceeding the thickness of the plate, FSDT can only predict a linear relation between the force and deflection. In reality, whether a plate is under static indentation, or large mass impact, membrane effects will occur for large deflections relative to the plate thickness. However, for sufficiently thick laminates, the onset of

membrane effects can be delayed. In a series of experiments by Seamone [3], low velocity impacts were conducted on thin and thick laminates to study the effects of barely visible impact damage on load carrying capabilities. A comparison of the force-deflection plots for thin and thick laminates can be seen in Figure 3.11.

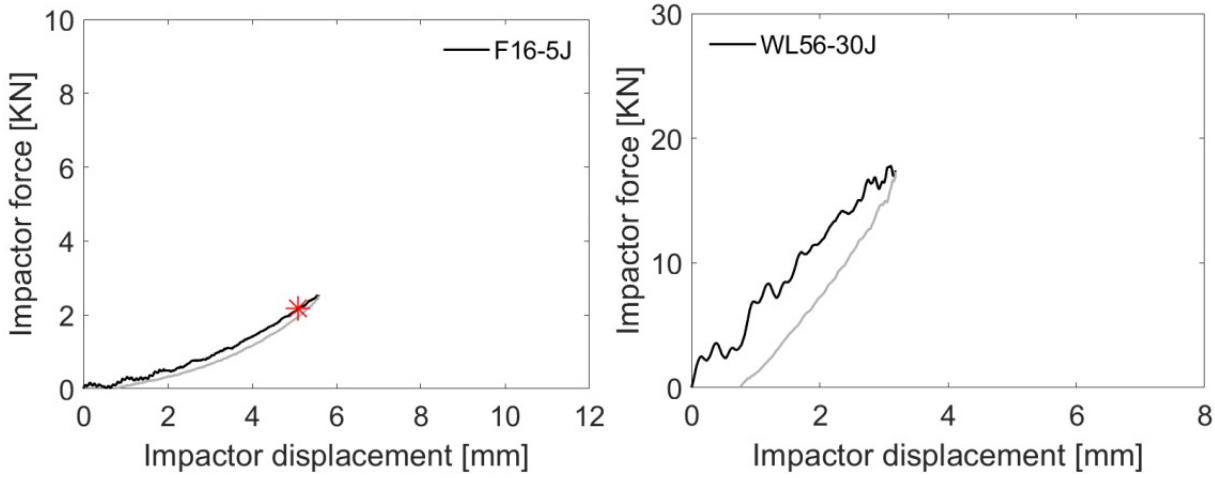

(a) Impact on 16 Ply Laminate (b) Impact on 56 Ply Laminate

Figure 3.10: Force-Deflection Plots for a Thin and Thick Laminate [3]

On the 16 ply laminate, nonlinear behavior is strongly evident. On the 56 ply laminate, the behavior of the force-deflection plot is mostly linear due to the greater thickness of the laminate. Because of the inability of FSDT to model the nonlinear large deflection behavior, the scope of the comparison study between the dynamic impact and static indentation models is restricted to the linear response region.

3.6 Linear Response Region

Because the scope of the study is restricted to the linear response region, it is necessary to define this region. Consider a 20 J impact on a 32 ply 150 mm x 150 mm laminate. A comparison of the force-deflection curves for this impact using the two degree of freedom spring mass model and FSDT for a CPL is shown in Figure 3.11.

From the figures, it can be seen that the force-deflection curves closely follow the same path for deflections below about 1.1 mm. Beyond this deflection, membrane effects become significant drastically increasing the amount of force necessary to produce addi-

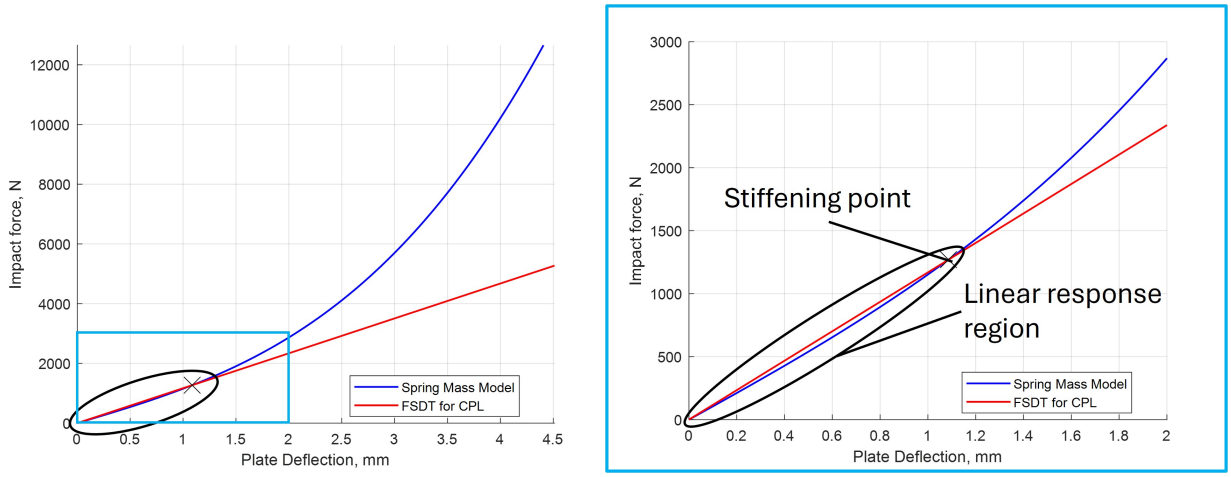

(a) Force-Deflection Plot (b) Linear Response Region

Figure 3.11: Comparison of Force-Deflection

tional bending and the models diverge. Based on the force-deflection plots of the two models alone, within the linear response region it can be safely stated that static indentation provides a reasonable substitute for large mass low velocity impacts. Beyond the linear response region, it is uncertain if static indentation will produce similar responses to impact testing.

The linear response region is defined as the portion of the force-deflection plot from zero deflection up until the point where the two curves cross. This cross over point is termed the stiffening point and defines the deflection and impact force at which membrane effects become significant. To determine when membrane effects are significant, force-deflection plots for the dynamic and static model are compared to see when they diverge.

3.7 Setup of the Analytical Study

The study is performed assuming a low velocity impact on a rectangular, simply supported and specially orthotropic plate. The material is assumed to be IM7/977-3. Properties for this material are shown below in Table 3.2.

In this study, the laminates are allowed to vary from 16 plys to 48 plys. The stacking sequences used are $(0/90)_{4s}$, $(0/90)_{5s}$, $(0/90)_{6s}$, $(0/90)_{7s}$, $(0/90)_{8s}$, $(0/90)_{9s}$, $(0/90)_{10s}$, $(0/90)_{11s}$, and $(0/90)_{12s}$. The laminate is assumed to be square and the side length of the

E_{11}	E_{22}	E_{33}	G_{12}	G_{13}	G_{23}	ν_{12}	K	t_{ply}	ρ_p
GPa	GPa	GPa	GPa	GPa	GPa	-	-	mm	kg/m^3
164.3	8.84	8.84	6.74	6.74	3.7	0.329	5/6	0.13	1580

Table 3.2: Material Properties of IM7/977-3 [3]

laminate is allowed to vary from 100 mm to 450 mm in increments of 50 mm. In practice, the dynamic model will approximate the square laminate as a circular laminate of equal area and plate radius $r_p = \sqrt{a^2/\pi}$. The impactor is assumed to have a spherical tip with a 1 inch diameter and is made of steel. The impactor properties and impact energy are shown below in Table 3.3. All impacts are performed using a 20 J impact to ensure that deflections occur beyond the stiffening point so that it can be identified in all impacts.

m_i	r_i	E_i	G_i	ν_i	Energy
kg	mm	GPa	GPa	-	J
5.5	12.7	199.95	75.17	0.33	20

Table 3.3: Impactor Properties and Impact Energy

MATLAB was used to implement the dynamic impact and static indentation models. Because the dynamic model requires that the applied loading and shear stiffness be calculated iterativly, a 4th order Runge-Kutta integration scheme was used to solve the dynamic model. The order of the analytical study is as follows.

1. The nonlinear dynamic model is initially solved for and is used to produce a force displacement plot.

2. The resulting applied loading from the dynamic model is used to produce a force displacement plot for the static model of a square plate using the FSDT solution.

3. The solution for the dynamic impact model is then repeatedly ran to solve for the impact energy which produces a maximum deflection at the stiffening point.

The study is performed using the above material properties in Tables 3.2 and 3.3. Throughout the study, the number of plys and laminate dimensions are allowed to change. For each laminate stackup, the effective plate stiffness is calculated to give a quantitative

understanding of how the number of plys affects the stiffness of the laminate. In some versions of the literature, the following equation is used to calculate the laminate stiffness [3, 12, 14, 15]

$$D^* = \sqrt{D_{11}D_{22}(A+1)/2} \quad A = (D_{12} + 2D_{66})/\sqrt{D_{11}D_{22}} \tag{3.51}$$

while in other versions, the equation shown below is used [18] [19].

$$D^* = \frac{1}{2}\left(D_{12} + 2D_{66} + \sqrt{D_{11}D_{22}}\right) \tag{3.52}$$

In this study, the stiffness given by equation 3.51 will be used.

The parameters of this study are the number of plys, from 16 to 48 plys, and the laminate side lengths, from 100 mm to 450 mm. To show that the use of quasi-static indentation is appropriate to model the impacts considered in this study, the 4 extreme cases of the parameters under consideration are plotted on the impact characterization diagram. The 4 extreme cases of the study are the 16 ply laminate with 100 mm side lengths and 450 mm side lengths, and the 48 ply laminate with 100 mm side lengths and 450 mm side lengths. These cases are plotted on the impact characterization diagram shown in Figure 3.12.

From the figure, it can be seen that impacts on the laminates with a 100 mm side length occur far into the quasi-static region. For these impacts, a great deal of overlap is expected to occur between the force-deflection plots for the dynamic impact and static indentation models. For impacts on the laminates of 450 mm side lengths, these impacts will still occur within the quasi-static region, but are much closer to the quasi-static boundary than the impacts on the laminates of 100 mm side lengths. Static indentation should still provide a good approximation of these impacts, but a smaller region of overlap between the two models is expected for these cases.

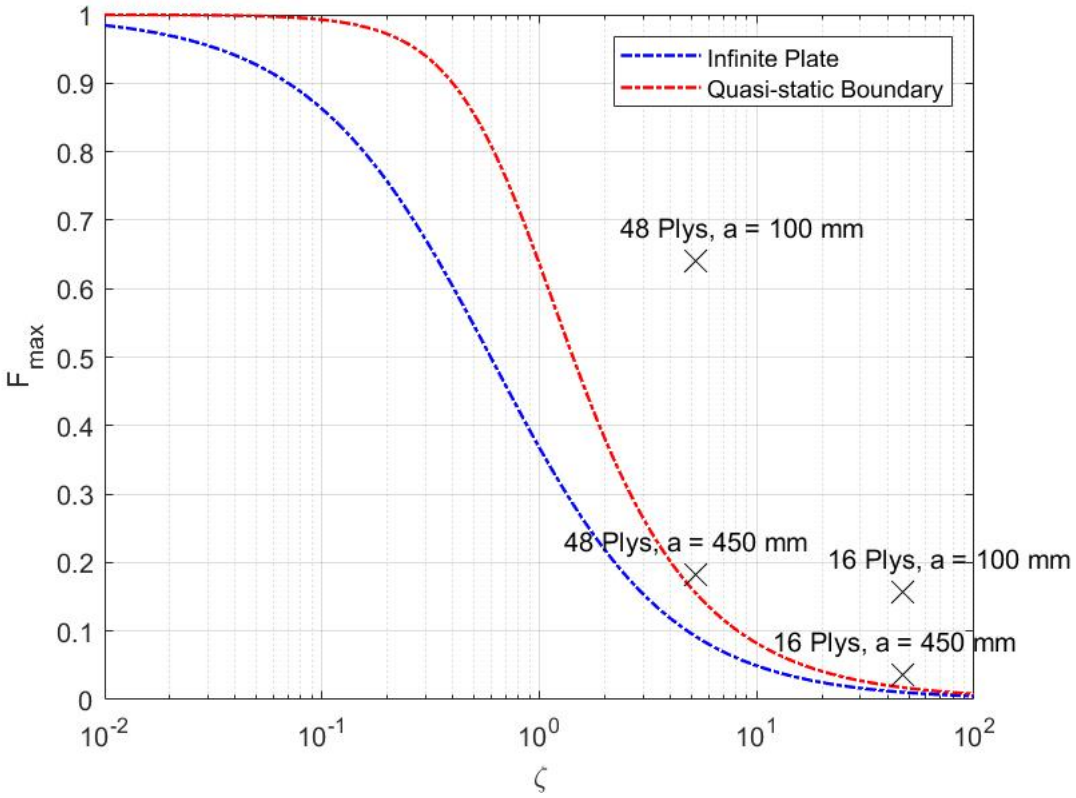

Figure 3.12: Characterization of Study Impacts

Chapter 4

Results

This chapter presents the results of the parametric study, with the effects of increasing side length and effective plate stiffness on the stiffening point and on the impact energy at which the stiffening point occurs. The possibility of using static indentation to induce first ply delamination is also discussed.

4.1 Comparison of the Dynamic and Static Model

72 different impact cases are considered in this study with the number of plys ranging from 16 to 48 plys and the side lengths ranging from 100 mm to 450 mm. For conciseness, the force-deflecton plots for 20 of the cases are shown here. The cases shown are the impacts performed on laminates of 16, 24, 32, 40, and 48 plys of side lengths 100, 200, 350, and 450 mm. The force-deflection plots for these impacts are shown in Figure 4.1 with the stiffening point indicated in each plot by the symbol $\times$.

From the plots, a strong overlap between the dynamic impact and static indentation model can be seen within the linear response region. Therfore, within the linear response region, it can be said that static indentation may potentially replace dynamic impact testing. This claim can be further validated with additional investigations into the damage formation of the two forms of testing.

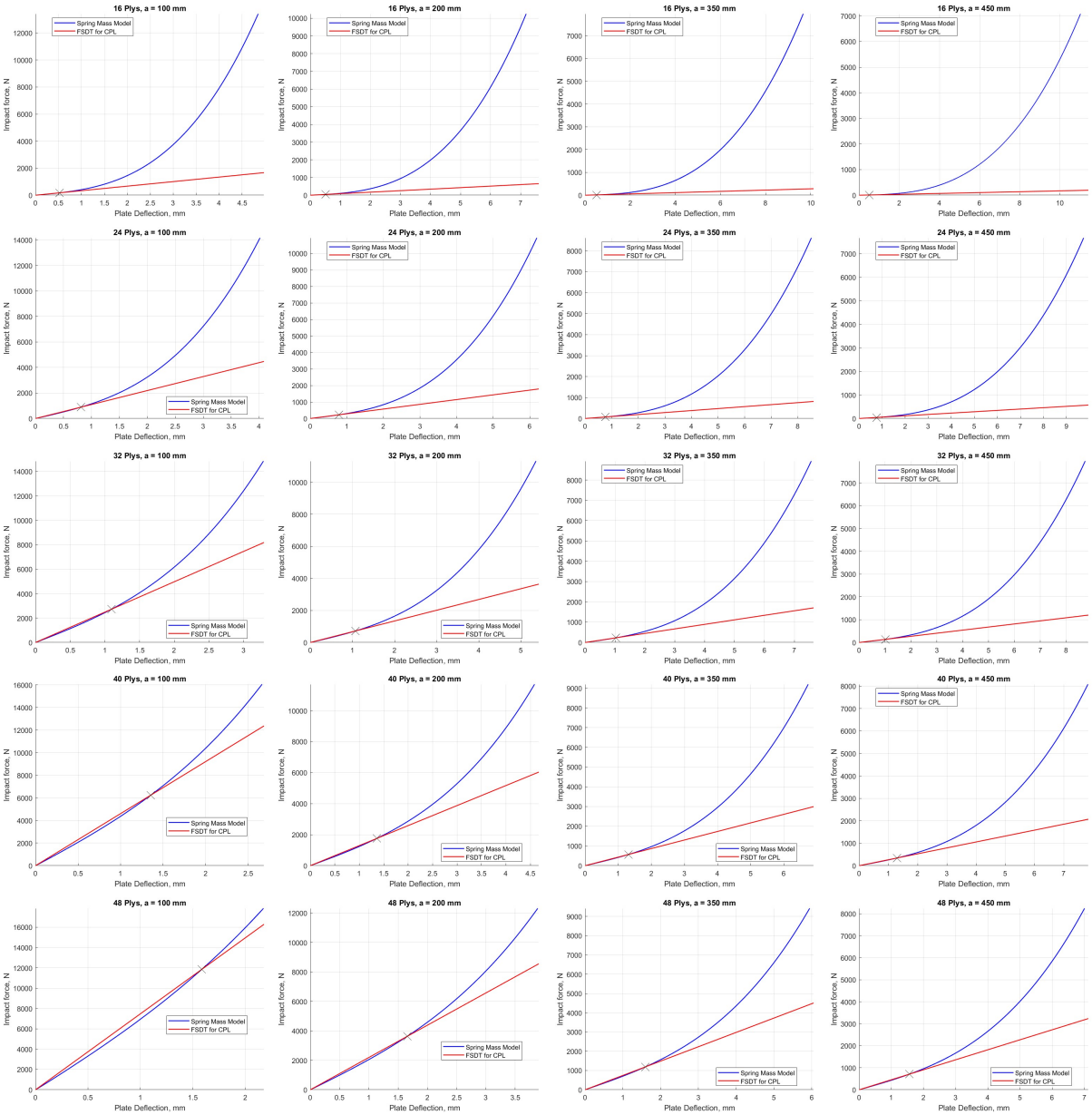

Figure 4.1: Comparison of Dynamic and Static Model Force-Deflection Curves

4.2 Effects of Increasing Side Length

The remainder of the study is dedicated to understanding how the chosen parameters affect the length of the linear response region. Increasing the plate side length or area has the effect of slightly decreasing the deflection at which the stiffening point occurs and reduces the impact force at the stiffening point. Consider a 16 ply and a 32 ply laminate, each of 150 mm side length, and another set of 300 mm side length. Figure 4.2 shows the force-deflection curves for the 150 mm side length set on the left and the 300 mm side length set on the right. From the figures, it can be seen that doubling the side length has a very minimal effect on the deflection at which stiffening occurs and drastically reduces the impact force. Additional stiffening points for laminates of other side lengths are shown in Table 4.1.

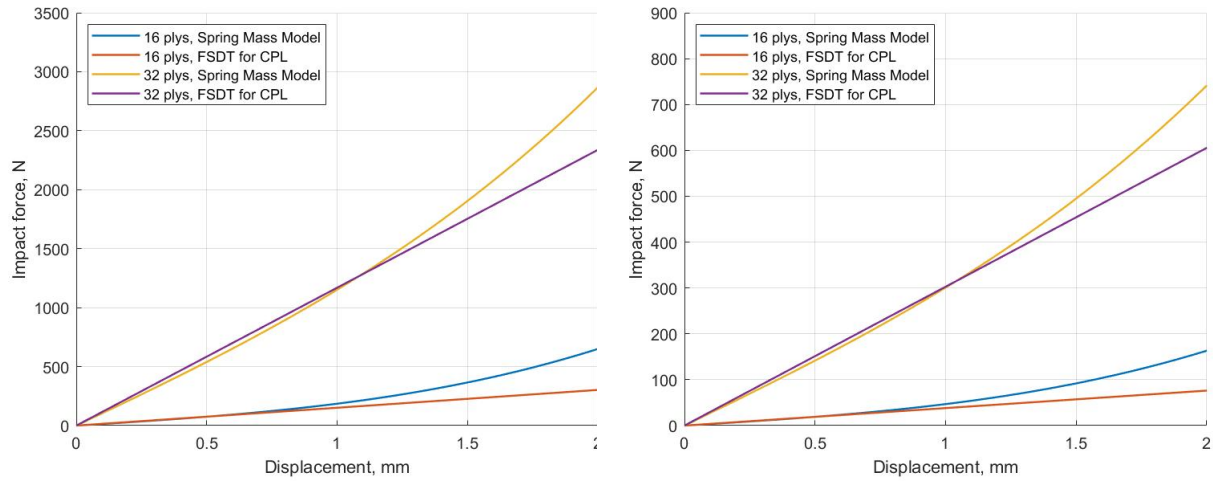

(a) $a = 150$ mm (b) $a = 300$ mm

Figure 4.2: Force-Deflection Curves for 16 and 32 Ply Laminates

From Table 4.1, moving from 150 mm side length to 300 mm, an increase in the laminate area by 4 times results in the impact force at stiffening decreasing by approximately 4 times. Similar results occur when moving from the 100 mm side length to 200 mm or moving from 200 mm to 400 mm. Slight decreases in the deflection at the stiffening point can be observed as the side length or area is increased. Increasing the laminate side length or area has the effect of slightly decreasing the deflection at the stiffening point and decreases the impact force at the stiffening point proportionally to the increase in

area. This effect occurs regardless of the effective plate stiffness.

		Stiffening Point									
Stacking	D*	$a = 100$ mm		$a = 150$ mm		$a = 200$ mm		$a = 300$ mm		$a = 400$ mm	
	N/m	mm	N	mm	N	mm	N	mm	N	mm	N
$(0/90)_{4s}$	49.7	0.524	175.5	0.513	77.5	0.505	43.2	0.499	19.0	0.496	10.7
$(0/90)_{8s}$	401.37	1.094	2721	1.087	1271	1.067	716	1.039	315	1.024	175

Table 4.1: Stiffening Point of a 16 and 32 Ply Laminate for Various Side Lengths

4.3 Effects of Increasing Effective Plate Stiffness

Increasing the number of plys or the effective plate stiffness causes an increase in both the deflection and impact force at which the stiffening point occurs. Consider a 20 ply and a 40 ply stacking sequence, each of 100 mm side length, and another set of 400 mm side length. Figure 4.3 shows the force-deflection curves for the 100 mm side length set on the left and the 400 mm side length set on the right. From the figures, it can be seen that doubling the number of plys roughly doubles the deflection at which the stiffening point occurs. A considerable increase in the impact force at the stiffening point can also be observed. Additional stiffening points for laminates of other stacking sequences are shown in Table 4.2.

From Table 4.2, moving from 20 to 40 plys, an increase in the effective plate stiffness by 8 times results in the deflection at stiffening to roughly double and the impact force at stiffening to increase by about 15 times. Similar results occur when moving from 16 to 32 plys or from 24 to 48 plys. A doubling in the number of plys or laminate thickness will result in the deflection at the stiffening point to roughly double and for the impact force to increase roughly between 14-16 times depending on the side length. These changes occur regardless of the laminate side length.

These effects of both the laminate side length and effective plate stiffness can be combined to produce a carpet plot of the stiffening point deflection and impact force. Figure 4.4 shows the carpet plots for the deflection at the stiffening point on the left and

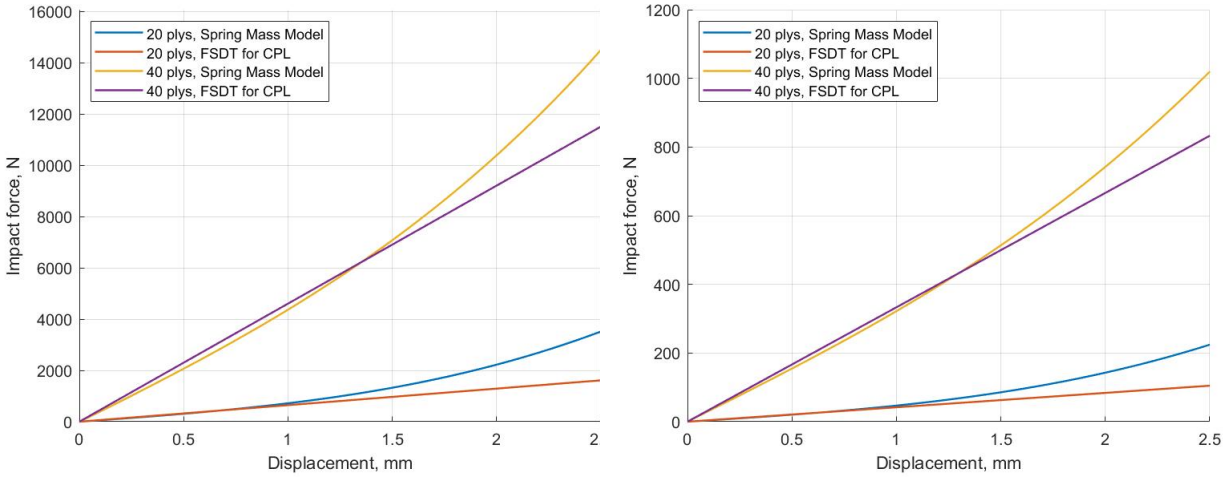

(a) $a = 100$ mm (b) $a = 400$ mm

Figure 4.3: Force-Deflection Curves for 20 and 40 Ply Laminates

		Stiffening Point			
Stacking Sequence	D*	$a = 100$ mm		$a = 400$ mm	
	N/m	mm	N	mm	N
$(0/90)_{4s}$	49.7	0.524	175.5	0.496	10.7
$(0/90)_{5s}$	97.5	0.668	431.0	0.626	26.3
$(0/90)_{6s}$	168.9	0.813	890.4	0.757	54.8
$(0/90)_{8s}$	401.4	1.094	2720	1.024	175.3
$(0/90)_{10s}$	784.9	1.354	6235	1.297	432.3
$(0/90)_{12s}$	1357	1.583	11843	1.577	903.8

Table 4.2: Stiffening Point of a 100 and 400 mm Side Length Laminate for Various Stacking Sequences

the impact force at stiffening on the right as functions of both the effective plate stiffness and side length.

From the figure on the left, it can be seen that increasing the laminate side length or area has a very minimal effect on the deflection at which stiffening occurs. Increases in the effective plate stiffness will increase the deflection at which the stiffening point occurs. From the figure on the right, it can be seen that decreases in side length and increases in effective plate stiffness will cause drastic increases on the impact force at which stiffening occurs.

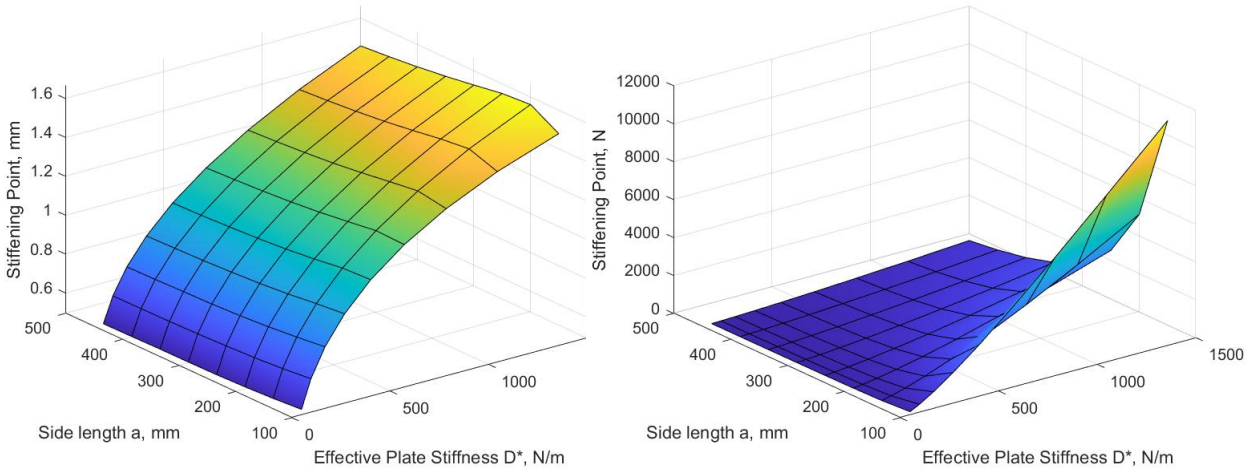

(a) Deflection at Stiffening (b) Impact Force at Stiffening

Figure 4.4: Deflection and Impact force at the Stiffening Point

4.4 Critical Impact Energy for Membrane Effects

The dynamic impact can be conducted repeatedly to solve for the critical impact energy at which the maximum impact deflection occurs at the stiffening point. This can be performed to determine the critical impact energy across all side lengths and stacking sequences. Any impacts performed at or below this critical impact energy will produce responses without significant membrane effects and may be approximated by static indentation. Consider a 44 ply laminate of 200 mm by 200 mm subject to a 20 J impact and the same laminate subject to a 1.827 J impact. The force-deflection plots for both impacts are shown in Figure 4.5.

From the plots, it can be seen that the 20 J impact produces significant nonlinear behavior beyond the stiffening point. However the impact response can be confined to the linear response region by reducing the impact energy below a critical level. Any impact can be confined to a linear response region by reducing the impact energy below a critical level. Figure 4.6 shows the critical impact energy where membrane effects begin to occur as a function of the laminate side length and effective plate stiffness.

Figure 4.6 closely resembles the carpet plot for the impact force at stiffening shown in Figure 4.4. Any decreases in laminate side length or area and increases in effective plate stiffness will cause drastic increases on the impact energy at which membrane stiffening

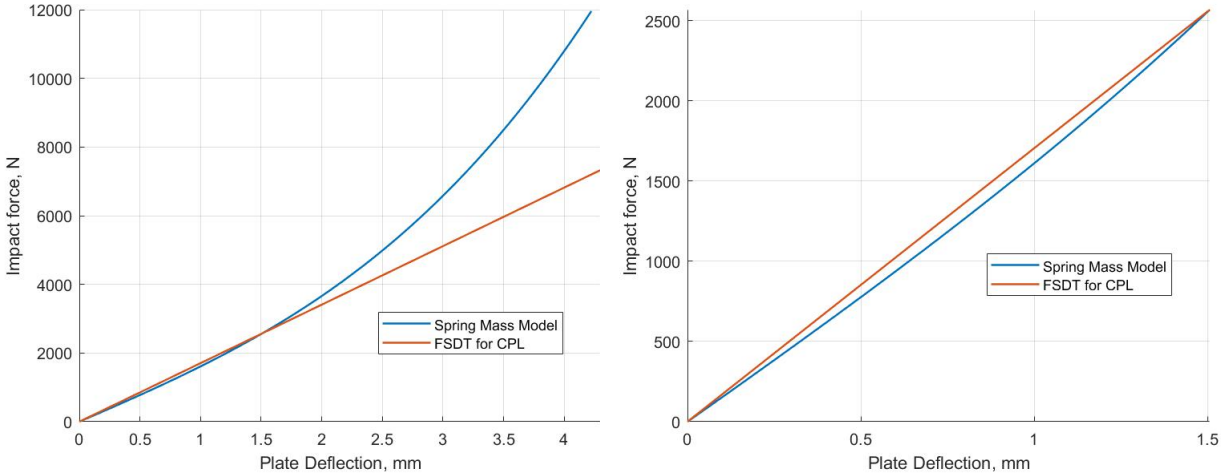

(a) KE = 20 J (b) KE = 1.872 J

Figure 4.5: Force-Deflection Curves for a 44 Ply Laminate

begins to occur. More precise changes in the critical impact energy can be seen in Table 4.3.

		Critical Impact Energy		
Stacking Sequence	D*	a = 100 mm	a = 200 mm	a = 400 mm
	N/m	J	J	J
$(0/90)_{4s}$	49.7	0.048	0.011	0.003
$(0/90)_{5s}$	97.5	0.148	0.035	0.009
$(0/90)_{6s}$	168.9	0.382	0.091	0.020
$(0/90)_{8s}$	401.4	1.678	0.389	0.094
$(0/90)_{10s}$	784.9	4.797	1.225	0.276
$(0/90)_{12s}$	1357	10.95	3.029	0.746

Table 4.3: Critical Impact Energy of Various Laminates

From the table, it can be seen that doubling the laminate side length or increasing the area by 4 times results in the critical impact energy to decrease by roughly 3.5 - 4.5 times depending on the effective plate stiffness. Doubling the number of plys or increasing the effective plate stiffness by roughly 8 times results in the critical impact energy to increase by over 30 times.

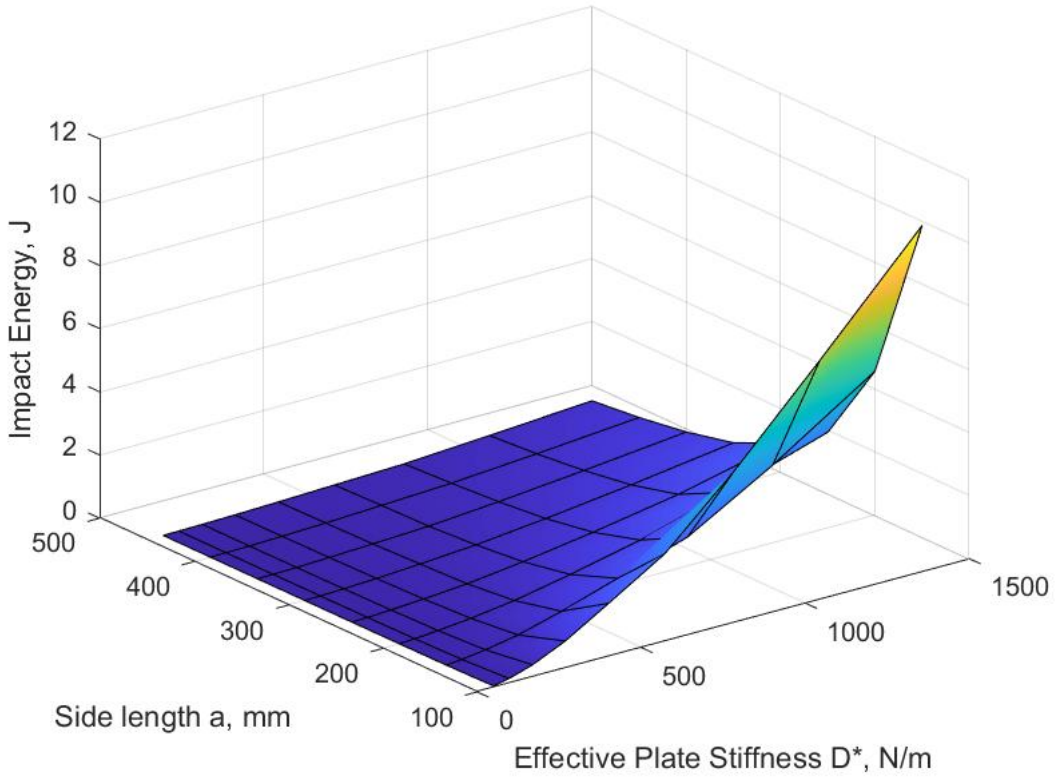

Figure 4.6: Critical Impact Energy at the Stiffening Point

4.5 Prediction of First Ply Delamination

The primary goal of Low Velocity Impact experiments is typically to test for impact resistance, or to initiate delamination to test damage tolerance. Substitution of LVI experiments with static indentation may be desirable when static indentation can be used to initiate delamination as low velocity impacts would. Olsson developed an analytical solution to predict the critical threshold load for delamination of specially orthotropic laminates based on the effective plate stiffness and mode II fracture toughness [14].

$$F_{cr} = \pi\sqrt{32D^{*}G_{IIC}/(n+2)} \tag{4.1}$$

Here, D* is the effective plate stiffness, G_{IIC} is the fracture toughness in pure mode II testing, and n is the number of delaminations. For first ply delamination, n is 1. Several values for the mode II fracture toughness of IM7/977-3 have been posted in the literature, some of which are shown in Table 4.4.

Material	$G_{IIC}, J/m^2$
	580
IM7/977-3	896
	607

Table 4.4: Mode II Fracture Toughness of IM7/977-3 [5] [6] [7]

Assuming an average value for the mode II fracture toughness of 694 J/m^2, the threshold force for delamination of the specially orthotropic laminates can be plotted as a function of the effective plate stiffness along with the impact force at the stiffening point for the different laminate configurations.

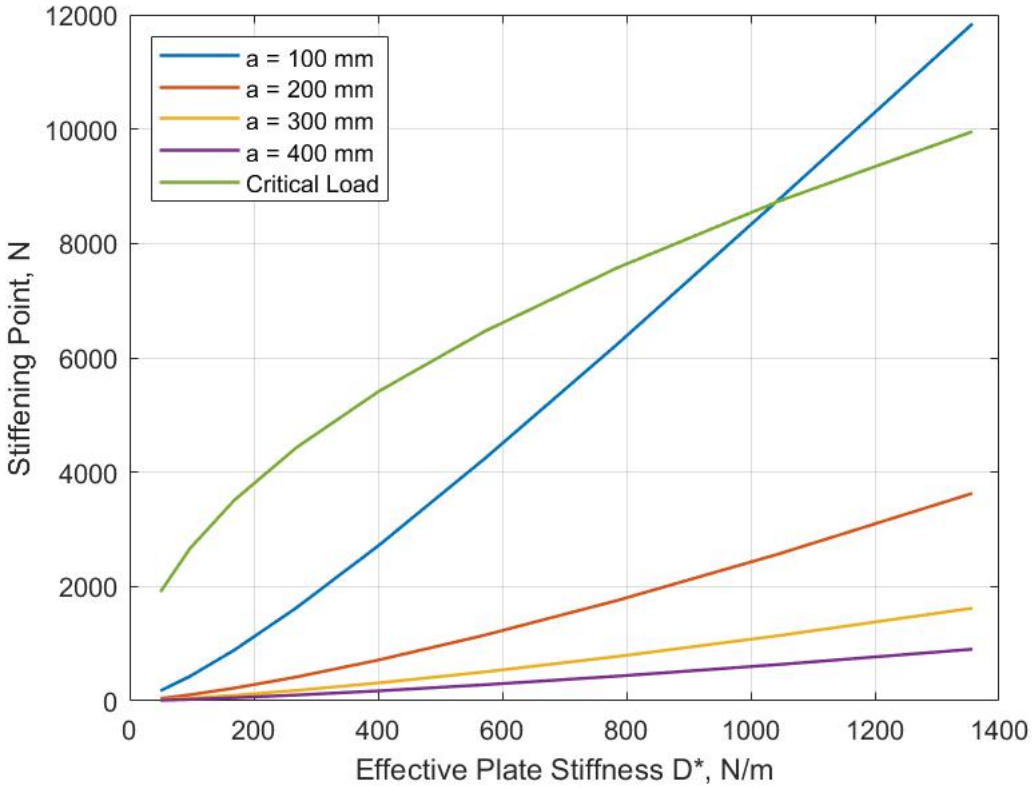

Figure 4.7: Critical Load for Delamination

From Figure 4.7, it can be seen that there is a small window where the impact force at stiffening exceeds the threshold force for first ply delamination for the 100 mm side length configuration beginning around 1040 N/m effective plate stiffness. This result indicates that for thick laminates of small side lengths or small areas, static indentation may potentially be used to initiate delamination.

Chapter 5

Conclusions and Recommendations for Future Work

In this study, a dynamic and static indentation model were compared to study the conditions under which similar responses were produced for the purpose of potentially substituting dynamic impact testing with static indentation. The models used throughout the study are a two degree of freedom spring mass model to simulate a low velocity impact and the application of the First order Shear Deformation Theory for a central point load to simulate the static indentation over a simply supported and specially orthotropic square laminate. The study found that there is a linear response region where both models produce similar results up to a certain point called the stiffening point. Beyond the stiffening point, membrane effects within the laminate become significant, drastically increasing the force necessary to produce additional bending within the dynamic impact model and the two models diverge. This divergence in the models occurs due to the inability of FSDT to capture membrane stiffening effects limiting the results of the study to the linear response region. Within the linear response region, the two models give approximately the same results. Based on the force-deflection plots, static indentation may potentially be used as a substitute to large mass low velocity impact testing. This claim can be further validated with investigations into the damage formation of the two forms of testing.

The linear response region of the spring mass model is defined as the portion of the force-deflection plot from zero deflection up until the point where the two curves cross. This cross over point is termed the stiffening point and defines the deflection and impact force at which membrane effects become significant. To determine when membrane effects are significant, force-deflection plots for the dynamic and static model were compared to see when they diverge. The stiffening point is characterized by both the deflection and impact force at which the models diverge. The effects of the parameters studied on the stiffening point are the effects of increasing laminate side length (or area) and the effects of increasing effective plate stiffness caused by increasing the number of plys in the laminate.

Increasing the laminate side length or area was found to slightly decrease the deflection at the stiffening point and to decrease the impact force at the stiffening point proportionally to the increase in the laminate area. For example, a doubling in the laminate side length will result the laminate area increasing by 4 times, and results in the impact force at stiffening to decrease by roughly 4 times. Increasing the effective plate stiffness was found to increase the deflection and impact force at the stiffening point. A doubling in the number of plys will increase the effective plate stiffness by 8 times, and roughly doubled the deflection at the stiffening point. An 8 fold increase in the effective plate stiffness was also found to increase the impact force at the stiffening point by roughly 14 - 16 times depending on the laminate side length.

The critical impact energy which produces a maximum deflection at the stiffening point was also studied. It was found that doubling the number of plys or increasing the effective plate stiffness 8 fold resulted in an over 30 fold increase in the impact energy at which the maximum deflection occurs at the stiffening point. Doubling the side length, or increasing the laminate area by 4 times was found to roughly decrease the critical impact energy by 3.5 - 4.5 times depending on the effective plate stiffness.

Lastly, the possibility of using static indentation to initiate delamination was also explored. An analytical solution was used to predict the threshold load to initiate first ply delamination. It was found that for high effective plate stiffness (1040 N/m) and

small side lengths (100 mm x 100 mm), there was a small region where the impact force at the stiffening point exceeded the threshold load for first ply delamination. This result indicates that delamination could potentially occur within the linear response region using static indentation.

The results of the study are restricted to the linear response region. Future studies could employ large deflection models to extend results into the nonlinear response region. The laminates involved in this study were restricted to simply supported and specially orthotropic laminates. Future work could extend the study to additional boundary conditions and other classes of laminates, such as quasi-isotropic or antisymmetric laminates. This study also assumed elastic responses and neglected material damage. Future studies could extend responses to include material damage. The models involved in this study were restricted to analytical models. Future work could expand the study to include finite element analysis or experimental impact testing and static indentation testing to validate the models developed.

Bibliography

[1] K. K. Singh and M. Shinde. *Impact Behavior of Fibre Reinforced Laminates*. Springer, 2022.

[2] A. S. Yigit and A. P. Christoforou. Limits of asymptotic solutions in low-velocity impact of compsoite plates. *Composite Structures*, 81(4):568–574, 2007.

[3] A. Seamone, P. Davidson, A. M. Waas, and V. Ranatunga. Low velocity impact and compression after impact of thin and thick laminated carbon fiber composite panels. *International Journal of Solids and Structures*, 292, 2024.

[4] K. N. Shivakumar, W. Elber, and W. Illg. Prediction of impact force and duration due to low-velocity impact on circular composite laminates. *Journal of Applied Mechanics*, 52(3):674–680, 1985.

[5] J. Zhang and X. Zhang. An efficient approach for predicting low-velocity impact force and damage in composite laminates. *Composite Structures*, 130:85–94, 2015.

[6] S. Lin, V. Ranatunga, and A. M. Waas. Computational study on the low velocity impact (lvi) of laminated composites with panel size effects. *Composite Structures*, 306, 2023.

[7] P. Shabani, L. Li, J. Laliberte, G. Qi, D. Rapking, and D. Mollenhaur. High-fidelity simulation of low-velocity impact damage in fiber-reinforced composite laminates using integrated discrete and continuum damage models. *Composite Structures*, 313:116910, 2023.

[8] R. Bogenfeld, J. Kreikemeier, and T. Wille. Review and benchmark study on the analysis of low-velocity impact on composite laminates. *Engineering Failure Analysis*, 86:72–99, 2018.

[9] ASTM D7136-15 Standard test method for measuring the damage resistance of a fiber-reinforced polymer matrix composite to a drop-weight impact event. ASTM Int 2015.

[10] S. Abrate. Modeling of impacts on composite structures. *Composite Structures*, 51(2):129–138, 2001.

[11] M. O. Pierson and R. Vaziri. Analytical solution for low-velocity impact response of composite plates. *AIAA Journal*, 34(8):1633–1640, 1996.

[12] E.V. Gonzalez, P. Maimi, P.P. Camanho, C.S. Lopes, and N. Blanco. Effects of ply clustering in laminated composite plates under low-velocity impact loading. *Composites Science and Technology*, 71(6):805–817, 2011.

[13] R. Olsson. Impact response of composite laminates - a guide to closed form solutions. Technical Report FFA TN 1992-33, Flygteksnika Forsoksanstalten, 1992.

[14] R. Olsson. Analytical prediction of large mass impact damage in composite laminates. *Composites Part A: Applied Science and Manufacturing*, 32(9):1207–1215, 2001.

[15] R. Olsson. Analytical prediction of damage due to large mass impact on thin ply composites. *Composites Part A: Applied Science and Manufacturing*, 72:184–191, 2015.

[16] J. N. Reddy. *Mechanics of Laminated Composite Plates and Shells: Theory and Analysis*. CRC Press, 2003.

[17] A.C. Ugural. *Plates and Shells: Theory and Analysis, Fourth Edition*. CRC Press, 2017.

[18] A. P. Christoforou and A. S. Yigit. Characterization of impact in composite plates. *Composite Structures*, 43(1):15–24, 1998.

[19] A. P. Chrsitoforou and A. S. Yigit. Effect of flexibility on low velocity impact response. *Journal of Sound and Vibration*, 217(3):563–578, 1998.